

Key Points:

- Spectral analysis of exclusively aeromagnetic data over East Antarctica provides new Curie Point Depth and geothermal heat flow estimates
- High heat flow imaged beneath the Transantarctic Mountains reinforces the hypothesis that the topography is thermally supported
- Using exclusively airborne data improves the resolution of Curie depth estimation, revealing heat flow correlated to geological features

Supporting Information:

Supporting Information may be found in the online version of this article.

Correspondence to:

M. Lowe,
maxwe32@bas.ac.uk

Citation:

Lowe, M., Mather, B., Green, C., Jordan, T. A., Ebbing, J., & Larter, R. (2023). Anomalously high heat flow regions beneath the Transantarctic Mountains and Wilkes subglacial basin in East Antarctica inferred from Curie depth. *Journal of Geophysical Research: Solid Earth*, 128, e2022JB025423. <https://doi.org/10.1029/2022JB025423>

Received 15 AUG 2022

Accepted 22 DEC 2022


Author Contributions:

Conceptualization: Maximilian Lowe
Data curation: Maximilian Lowe
Formal analysis: Maximilian Lowe, Chris Green, Tom A. Jordan
Funding acquisition: Robert Larter
Investigation: Maximilian Lowe, Robert Larter
Methodology: Maximilian Lowe, Ben Mather, Chris Green, Tom A. Jordan, Jörg Ebbing
Project Administration: Robert Larter
Software: Maximilian Lowe, Ben Mather

© 2022. The Authors.

This is an open access article under the terms of the [Creative Commons Attribution License](https://creativecommons.org/licenses/by/4.0/), which permits use, distribution and reproduction in any medium, provided the original work is properly cited.

Anomalously High Heat Flow Regions Beneath the Transantarctic Mountains and Wilkes Subglacial Basin in East Antarctica Inferred From Curie Depth

Maximilian Lowe^{1,2} , Ben Mather³ , Chris Green⁴ , Tom A. Jordan¹ , Jörg Ebbing⁵ , and Robert Larter¹ 

¹British Antarctic Survey, Cambridge, UK, ²The University of Edinburgh, Edinburgh, UK, ³The University of Sydney, Sydney, Australia, ⁴University of Leeds, Leeds, UK, ⁵Christian-Albrechts-Universität zu Kiel, Kiel, Germany

Abstract The Transantarctic Mountains (TAMs) separate the warmer lithosphere of the Cretaceous-Tertiary West Antarctic rift system and the colder and older provinces of East Antarctica. Low velocity zones beneath the TAM imaged in recent seismological studies have been interpreted as warm low-density mantle material, suggesting a strong contribution of thermal support to the uplift of the TAM. We present new Curie Point Depth (CPD) and geothermal heat flow (GHF) maps of the northern TAM and adjacent Wilkes Subglacial Basin (WSB) based exclusively on high resolution magnetic airborne measurements. We find shallow CPD and high GHF beneath the northern TAM, reinforcing the hypothesis of thermal support of the topography of the mountain range. Additionally, this study demonstrates, that limiting spectral analysis to areas with a high density of aeromagnetic measurements increases the resolution of CPD estimates revealing localized shallow CPD and associated high heat flow in the Central Basin of the WSB and the Rennick Graben (RG). Across the study area the CPD ranges from 15 to 35 km and the GHF values range from 30 to 110 mW/m². The recovered CPD range is compatible with recent Moho depth estimates, as the CPD predominantly lies within the crust, rather than in the magnetite-poor mantle. GHF estimates, based on the CPD estimates, show a good agreement to sparse in situ GHF measurements and the location of active volcanoes. Comparison to existing continent-wide GHF estimates shows strong differences from magnetically-derived heat flow estimates, while seismologically-derived heat flow estimates show the best agreement to our results.

Plain Language Summary The Transantarctic Mountains (TAMs) separating the ancient East Antarctic region from the younger West Antarctic region. Recent studies found regions where acoustic waves move slowly beneath the TAM. Slow wave speeds are considered to be caused by warmer rocks at depth, which provide thermal support for the TAM. We present heat flow maps for this region. The estimated heat flow is based on “Curie Point Depths” (CPDs), which describes the depth at which magnetic rocks lose their magnetic properties due to increasing temperature. This temperature is called the Curie temperature (~580°C for magnetite, the most common magnetic mineral in the Earth’s crust). The heat flow at the surface is estimated from the depth at which this temperature is reached. We use for the first time for a CPD study in Antarctica exclusively high-resolution magnetic data measured from aircraft. We demonstrated that limiting this method to airborne data improves the resolution of CPD variation, and thus heat flow estimates, substantially. We find shallow CPD and high heat flow beneath the TAM, which supports the suggestion that warmer rocks provide thermal support for the TAM. Additionally, we find high heat flow in the adjacent Wilkes Subglacial Basin and Rennick Graben.

1. Introduction

The evolution of both the Transantarctic Mountains (TAMs) and Wilkes Subglacial Basin (WSB) (Figure 1) as well as their coupling are not fully resolved, despite their crucial role in potential future sea level rise (DeConto & Pollard, 2016; Ferraccioli, Armadillo, Zunino, et al., 2009; Hansen et al., 2016; Jordan et al., 2013; Paxman et al., 2019).

The TAMs are the largest non-contractional mountain range on Earth (Figure 1), which divide East Antarctica from the West Antarctic Rift System (Morelli & Danesi, 2004; Robinson & Spletstoeser, 1986; Ten Brink & Stern, 1992). The approximately 4,000 km long and up to 400 km wide mountain range, with a peak elevation of 4,000 m (Morlighem et al., 2020), has a complex tectonic history with numerous proposed uplift mechanisms.

Supervision: Chris Green, Tom A. Jordan, Jörg Ebbing, Robert Larter
Validation: Maximilian Lowe, Chris Green, Tom A. Jordan, Jörg Ebbing, Robert Larter
Visualization: Maximilian Lowe
Writing – original draft: Maximilian Lowe
Writing – review & editing: Maximilian Lowe, Ben Mather, Chris Green, Tom A. Jordan, Robert Larter

Uplift models include flexural uplift (Paxman et al., 2019; ten Brink et al., 1997; Wannamaker et al., 2017; Yamasaki et al., 2008), thermal mantle support (Brenn et al., 2017; Lawrence et al., 2006; Smith & Drewry, 1984) as well as density variation and crustal thickening (Bialas et al., 2007; Huerta, 2007). A local study investigating crustal structures beneath the northern TAM based on receiver function data concluded that the crust beneath the TAM is up to ~46 km thick, which is significantly less than the 57 km required to support the mountains isostatically (Hansen et al., 2016). They instead suggest broad flexure of the East Antarctic lithosphere and uplift along the western edge as a result of lateral heat conduction from the hotter West Antarctic mantle in line with the uplift model by Stern & ten Brink (1989); ten Brink et al. (1997); ten Brink & Stern (1992). Recent studies based on new seismic tomography models (Brenn et al., 2017; Graw et al., 2016; Lloyd et al., 2020; Shen et al., 2018; Wiens et al., 2021) show large low velocity zones beneath the northern TAM, which are interpreted as warm and less dense mantle material. This observation suggests that the warmer mantle beneath the highest topographic features in Northern Victoria Land, provides a strong contribution of thermal support to the uplift of this region (Wiens et al., 2021).

The WBS located in the hinterland of the TAM, is a major below sea level topographic feature, buried 2–3 km beneath the East Antarctic Ice Sheet (EAIS) (Figure 1). The WBS was first described from radar data in the 1970s (Drewry, 1976) and stretches approximately 1,600 km from the George V Coast toward South Pole. The WBS comprises one of the largest marine-based sectors of the EAIS (Ferraccioli, Armadillo, Jordan, et al., 2009; Ferraccioli, Armadillo, Zunino, et al., 2009). The bedrock elevation reaches depths of more than 2,000 m below sea level within the locally more deeply incised sub-basins (Ferraccioli, Armadillo, Jordan, et al., 2009; Morlighem et al., 2020). The WBS is about 600 km wide close to the George V coast (Ferraccioli, Armadillo, Zunino, et al., 2009), decreasing to <100 km toward South Pole (Studinger et al., 2004). The modern landscape formation of the WBS is interpreted as being associated with flexural process of the TAM uplift and glacial erosion (Ferraccioli, Armadillo, Jordan, et al., 2009; Jordan et al., 2013; Paxman et al., 2018; Paxman et al., 2019). The WBS is bounded by the Terre Adélie Craton, West of the Mertz shear zone (Finn et al., 2006) and by the TAM on the East. Direct information about the subglacial geology is limited to rock exposure close to the coast. West of the Mertz shear zone $\geq 2,440$ Ma paragneiss and granitoids have been reported, while to the east ca. 500 Ma granites have been mapped (Goodge & Fanning, 2010). Evidence exists for ~680 Ma rifted margin in the central TAM (Goodge, 2020), and extensive Ross age (550–500 Ma) magmatism in the TAM (Lamarque et al., 2018). The presence of Beacon Super group sedimentary strata intruded by rocks of the Ferrar Large Igneous Province within the WBS are interpreted from aeromagnetic measurements (Ferraccioli, Armadillo, Jordan, et al., 2009). Provenance studies also indicate the bedrock of the WBS includes Beacon Supergroup terrestrial sediments, rocks of the Ferrar Large Igneous Province, and Early Paleozoic terranes (Cook et al., 2017).

Basins below sea level like the WBS pose a potentially high, but poorly constrained risk for future sea level rise, as they are more vulnerable to melting by warming of the surrounding ocean. Such melting could potentially trigger mechanisms of unstable retreat (Pollard et al., 2015; Schoof, 2007). Significant long-term contribution is predicted from the WBS region to future sea-level rise over the next two centuries and eventual retreat of the ice sheet into the northern WBS by the year 2,500 (DeConto & Pollard, 2016; Stokes et al., 2022). Geothermal heat flow (GHF) is identified as a crucial contribution from the solid Earth which interacts with the cryosphere (Davies, 2013; Fahnestock et al., 2001). GHF influences the rheology of the ice and can lead to basal melting, factors which can both facilitate enhanced ice flow and consequently influence ice sheet stability (Larour et al., 2012; Llubes et al., 2006; Pittard et al., 2016; Winsborrow et al., 2010). GHF is therefore a crucial parameter for modeling ice sheets and future sea-level rise (Matsuoka et al., 2012; Pattyn, 2010; Pattyn et al., 2016; Pittard et al., 2016; Van Liefferinge et al., 2018; Whitehouse et al., 2019; Winkelmann et al., 2011). GHF also has the potential to shed light on the region's long-term tectonic evolution. Areas of elevated heat flow are often associated with regions of shallow warm mantle, and provide a test for the hypothesis that incursion of warmer West Antarctic mantle beneath the TAM provides thermal support to the mountain range, as suggested by (Hansen et al., 2016; Smith & Drewry, 1984)

Although in-situ GHF measurements would be very significant, they are almost non-existent (Burton-Johnson et al., 2020). Consequently, GHF models are inferred from different geophysical techniques. Those techniques can be subdivided into two broad categories: modeling of geophysical data and machine learning or statistical correlation. Modeling approaches include determining the depth of the 580°C isotherm from magnetic data and subsequently calculating GHF from this isotherm (Martos et al., 2017) as well as calculating GHF based on seismologically derived upper mantle temperature (An et al., 2015). Statistical models include correlating seismic

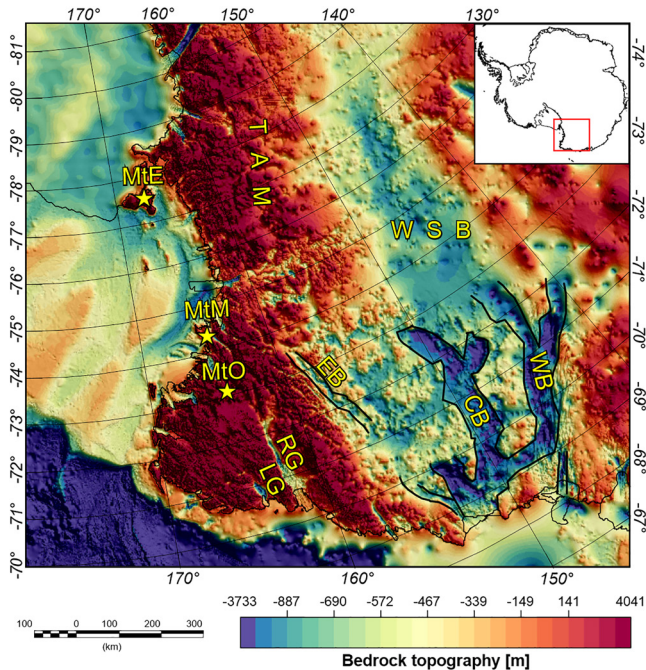


Figure 1. Bedrock topography of the Transantarctic mountains and Wilkes Subglacial Basin from the Bedmachine model version 2 (Morlighem et al., 2020). Black lines delimit more deeply incised sub-basins within the wider WBS region. Yellow stars indicate the location of recently active volcanoes. LG: Lillie Graben; RG: Rennick Graben; EB: Eastern Basin; CB: Central Basin; WB: Western Basin; WBS: Wilkes Subglacial Basin; TAM: Transantarctic Mountains; MtE: Mount Erebus; MtM: Mount Melbourne; MtO: Mount Overlord.

velocity structures in Antarctica to those in areas with good constraints on GHF (Shen et al., 2020), machine learning techniques where the model is trained in areas where the GHF is well understood (Lösing & Ebbing, 2021; Lösing et al., 2020) and statistical similarity of multiple data sets which are compared to global GHF catalogs (Stål et al., 2021). The large-scale distinction between East and West Antarctica is recognised in most GHF models (An et al., 2015; Lösing & Ebbing, 2021; Martos et al., 2017; Shen et al., 2020; Stål et al., 2021). However, existing continental scale GHF models for Antarctica show remarkable inconsistency on a more local scale (Figure 2).

In this study, in contrast to previous attempts to estimate Curie Point Depth (CPD) and GHF in Antarctica from spectral analysis of magnetic data, we use exclusively high resolution airborne magnetic data. Exclusive use of airborne data improved existing GHF models based on CPD significantly in the TAM and WBS area. We imaged elevated GHF beneath the northern most part of the TAM, which verifies independent seismological findings of proposed thermal support for uplift in northern Victoria Land (Hansen et al., 2016; Lloyd et al., 2020; Wiens et al., 2021). Furthermore, our study reveals elevated GHF in the WBS Central Basin (CB) and the Rennick Graben (RG) which previous models were not able to image, which is consistent with an erosional or rifted origin.

2. Data

The ADMAP-2 compilation includes 3.5 million line-km of aeromagnetic and marine magnetic data in Antarctica and the Southern Ocean south of 60°S (Golynsky et al., 2018). The gridded ADMAP-2 product (Figure 3a) has a grid spacing of 1.5 km and its production included correction for the International Geomagnetic Reference Field, diurnal effects correction, high-frequency error correction, leveling, regional gridding, and merging of regional grids into a continent-wide compilation (Golynsky et al., 2018).

For this study only recent (~2,000–present) aeromagnetic data was selected from ADMAP-2 and a blanking distance of 15 km from flight lines was applied (Figure 3b). This was done for two reasons: (a) To ensure that only flight lines with high precision positioning tracing (Global Positioning System) are used and (b) interpolation between widely spaced flight line spacing is removed. Data was re-interpolated onto a 1.5 by 1.5 km mesh using a minimum curvature technique. The resulting magnetic grid was then upward continued to a constant height of 4 km above the ellipsoid (Figure 3b), based on the flight elevation data available in the ADMAP-2 compilation (Section S1 in Supporting Information S1).

3. Method

Magnetic materials typically lose their magnetisation (ability to induce a strong magnetic field) with increasing temperature (Blakely, 1996; Langel & Hinze, 1998). For magnetite, thought to be the most significant magnetic mineral in the crust, this so-called Curie temperature is ~580°C (Telford et al., 1990). The depth at which the crust reaches this temperature, and most rocks lose their magnetic properties, is the CPD and defines the Curie isotherm within the crust (Haggerty, 1978; Núñez Demarco et al., 2020). Estimating the depth of magnetic sources using the power spectrum of magnetic data was first established as a method in 1970 (Spector & Grant, 1970). Since then, numerous methods were developed to estimate the bottom of all magnetic sources in an area, and hence the CPD. Established methods to estimate the CPD include the centroid method (Bhattacharyya & Leu, 1975a, 1975b; Blakely, 1996; Okubo et al., 1985; Tanaka et al., 1999; Treitel et al., 1971) spectral peak method (Blakely, 1996; Connard et al., 1983) and fractal methods (A. R. Bansal & Dimri, 2005; A. R. Bansal et al., 2011; Bouligand et al., 2009; Kumar et al., 2021; Li et al., 2019; Mather & Fulla, 2019; Maus & Dimri, 1995; Maus et al., 1997; Salem et al., 2014; Todoschuck et al., 1992) for a more detailed discussion of those methods the reader is referred to (Núñez Demarco et al., 2020; Ravat et al., 2007).

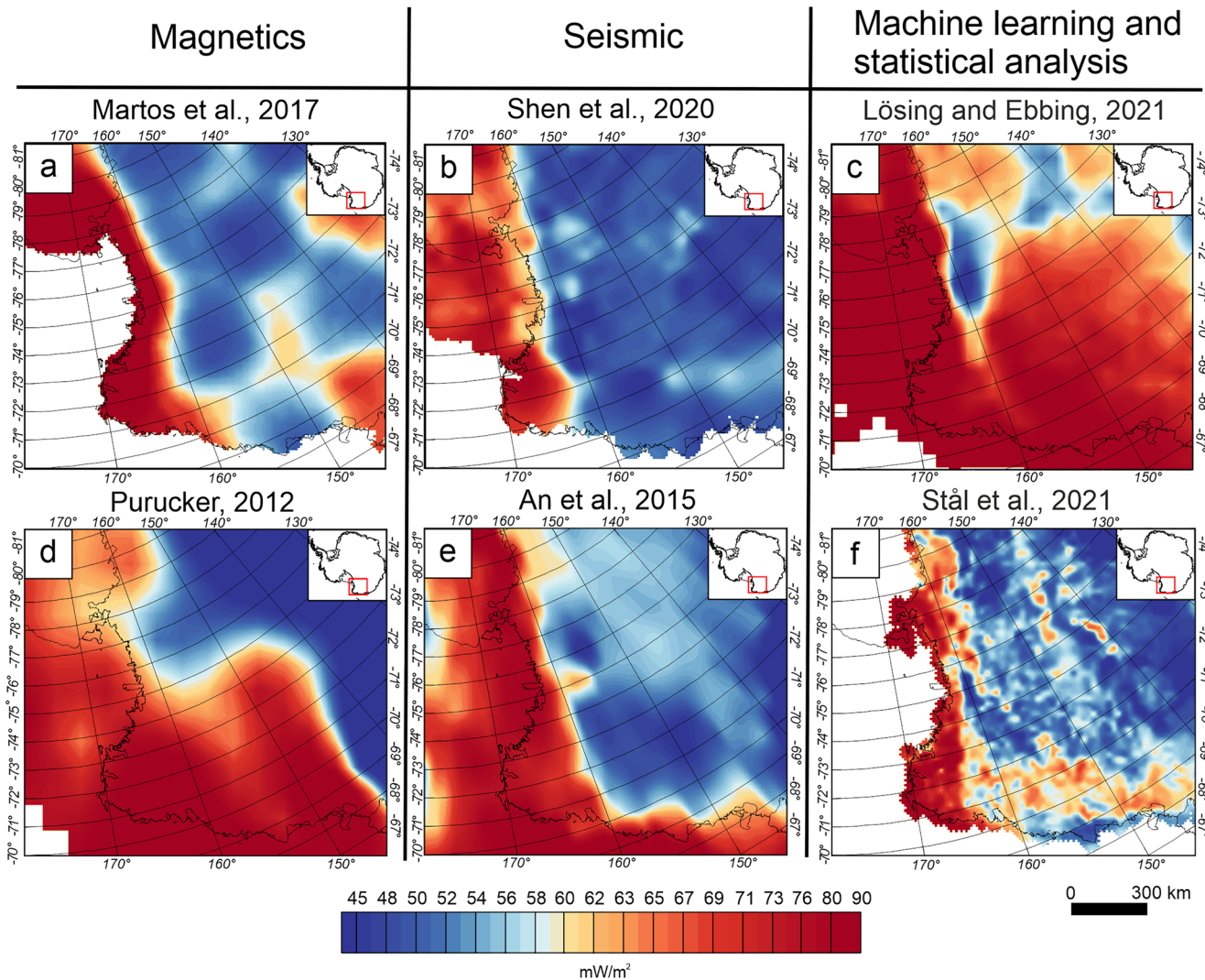


Figure 2. Continent-wide geothermal heat flow (GHF) models derived from various geophysical approaches. (a) Magnetic derived GHF model (Martos et al., 2017). (b) Seismological derived GHF model (Shen et al., 2020). (c) GHF model derived from multiple data sets via Machine Learning (Lössing & Ebbing, 2021). (d) GHF map derived from satellite magnetic data (Purucker, 2013) an update of Fox Maule et al. (2005) (e) Seismologically inferred GHF model (An et al., 2015). (f) GHF estimates derived by statistical analyses of multiple data sets (Stål et al., 2021). Identical colormap used for (a–f).

In our study the centroid method after (Tanaka et al., 1999) is used to calculate the CPD. This approach assumes a random distribution of magnetic sources in the crust. The radially averaged power spectrum was calculated using the python library Pycurious (Mather & Delhaye, 2019).

The radially averaged power spectrum $\Phi_{\Delta}(k)$ is defined as:

$$\Phi_{\Delta T}(|k|) = A e^{-2|k|Z_t} \left(1 - e^{-|k|(Z_b - Z_t)}\right)^2 \quad (1)$$

where A is a constant, k is the spatial wavenumber defined as $k = 2\pi/\lambda$, where λ is the wavelength), Z_t is the top of assumed magnetic source and Z_b is bottom of assumed magnetic source and therefore $Z_b - Z_t$ describes the thickness of the magnetic source (Mather & Delhaye, 2019; Tanaka et al., 1999).

For shorter wavelengths (generally less than twice the source thickness), this approximates to:

$$\ln[\Phi_{\Delta T}(|k|)^{\frac{1}{2}}] = \ln B - |k|Z_t \quad (2)$$

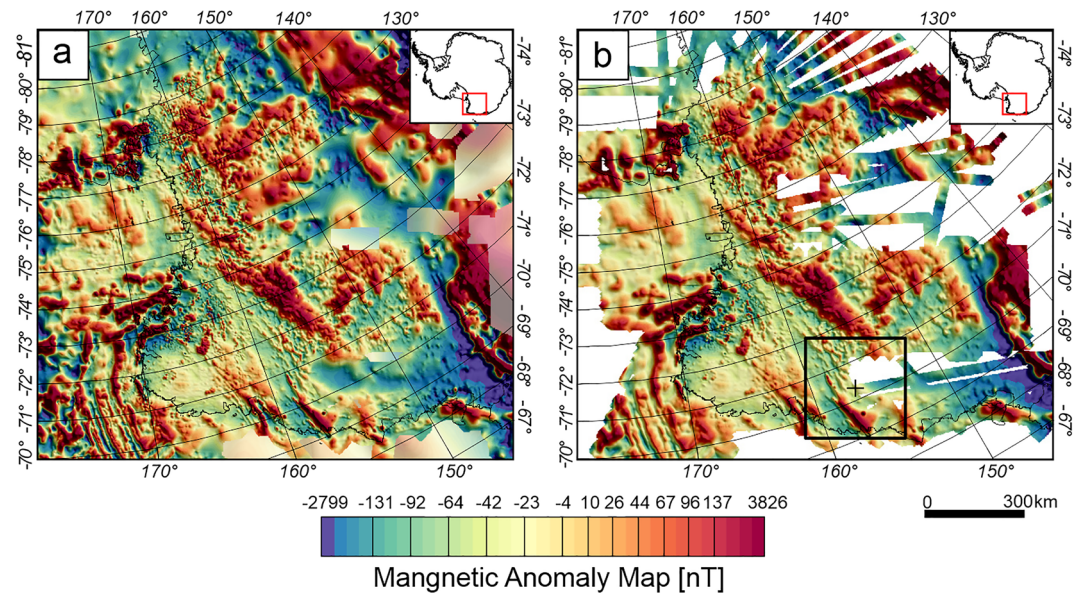


Figure 3. (a) ADMAP-2 with a grid spacing of 1.5 km (Golynsky et al., 2018) superimposed on Satellite Magnetic Anomaly Map from the Lithospheric model derived from CHAMP and Swarm satellite data, version 1 model (Olsen et al., 2017). (b) Selected recent ADMAP-2 magnetic data, which was re-gridded and upward continued to a constant height of 4 km. Black cross and black rectangle indicate the centroid and extension of window 645 with a window size of 300 km. Identical colormap used for (a and b).

where B is constant (Mather & Delhaye, 2019; Tanaka et al., 1999).

Equation 1 can be rewritten, with Z_0 as the centroid depth of the magnetic source (Mather & Delhaye, 2019; Tanaka et al., 1999).

$$\Phi_{\Delta T}(|k|)^{\frac{1}{2}} = C e^{-|k|Z_0} \left(e^{-|k|(Z_t - Z_0)} - e^{-|k|(Z_b - Z_0)} \right) \quad (3)$$

where C is a constant.

For long wavelengths, where $2d$ is the magnetic source thickness we obtain Equations 4 and 5 (Mather & Delhaye, 2019; Tanaka et al., 1999).

$$\Phi_{\Delta T}(|k|)^{\frac{1}{2}} = C e^{-|k|Z_0} \left(e^{-|k|(-d)} - e^{-|k|(d)} \right) \approx C e^{-|k|Z_0} 2|k|d \quad (4)$$

$$\ln \left\{ \frac{\Phi_{\Delta T}(|k|)^{\frac{1}{2}}}{|k|} \right\} = \ln D - |k|Z_0 \quad (5)$$

The depth to the top (Z_t) and centroid (Z_0) of the magnetic source are recovered by fitting a linear regression through the high-wavenumber and low-wavenumber part of the radially averaged spectrum of $\ln[\Phi_{\Delta T}(|k|)^{\frac{1}{2}}]$ and $\ln \left\{ \frac{\Phi_{\Delta T}(|k|)^{\frac{1}{2}}}{|k|} \right\}$ in Equations 2 and 5, respectively (Tanaka et al., 1999). With Z_t and Z_0 the base of the magnetic source (Z_b) can be estimated applying Equation 6 (Mather & Delhaye, 2019; Tanaka et al., 1999).

$$Z_b = Z_0 - (Z_t - Z_0) = 2Z_0 - Z_t \quad (6)$$

A random magnetization model was chosen over a fractal model first because recent CPD studies in Antarctic and Greenland (Dziadek et al., 2021; Martos et al., 2017; Martos et al., 2018) have used a random magnetisation

model and we want to obtain results that can be compared directly to previous studies. Second the subglacial geology in the area of the TAMs and WBS is largely unknown. A fractal magnetization model introduces a fractal exponent parameter β , which is related to geology (Bouligand et al., 2009). However, random magnetization is an endmember of the fractal magnetization model with fractal parameter $\beta = 1$ (Bouligand et al., 2009). For meaningful β values above 1 geological terrains need to be identified and constrained. Adding an unconstrained fractal parameter adds complexity which is difficult to tie down since different geological terrains would require different β values. Fixing β to a constant value as previous studies have done, for example, (Sobh et al., 2021) will not provide an advantage over a random magnetization model. A recent study illustrated the difficulty in estimating reliable β values and highlights the possibility that β is only valid in a limited bandwidth (Szwilius et al., 2022). To limit the complexity and ambiguity a fractal model would introduce, combined with ensuring comparability to previous Antarctic studies, we have chosen the standard approach of assuming random magnetization over a fractal model.

3.1. Data Preparation and Window Size

The window size is an influential parameter in spectral methods because it ultimately determines the maximum wavelength which will be captured in the subgrid and therefore controls the maximum depth that can be recovered (Núñez Demarco et al., 2020).

Various authors make conflicting suggestions regarding appropriate window sizes (Núñez Demarco et al., 2020) ranging from 3 times the depth of the magnetic layer (Hussein et al., 2013) to 10 times the recovered depth of the magnetic layer (Ravat et al., 2007). In contrast, Li et al. (2017) use several window sizes, where the recovered depths are averaged into the final CPD grid (Bouligand et al., 2009). use an iterative approach, where they expand the window around a given grid point until a depth of the bottom of the magnetic layer Z_b smaller than a tenth of the window size is recovered. In this study, we test recovery of the CPD beneath the TAM and WBS using analysis window sizes of 200 km by 200 km, 300 km by 300 km, and 400 km by 400 km following the recommendation for a window size of 5–10 times the recovered CPD (Ravat et al., 2007). We discuss the differences in absolute value, resolution and accuracy of recovered CPD, and justify our choice of a 300 km preferred window size later (Section 5).

The Fourier transformation requires the windowed data to have no data gaps. However, Antarctica is not fully covered by magnetic airborne surveys. Previous studies in Antarctica have bypassed this problem by merging the airborne data with satellite magnetic data (Dziadek et al., 2021; Martos et al., 2017). Satellite magnetic data for estimating CPD should be used with caution because the analytical window functions as a high pass filter removing all wavelengths longer than the window size. However, satellite derived magnetic models only contain longer wavelengths, similar in length to the typical analysis window, for example, the satellite derived magnetic model MF7 (Maus et al., 2007) contains only wavelength larger than 300 km. It is therefore questionable whether merged satellite and airborne magnetic data can provide a representative CPD estimation due to the limited wavelengths in the power spectrum. This issue was recently discussed by Pappa and Ebbing (2021). In our study the problem regarding data gaps within the airborne data is overcome by interpolation of the airborne data to ensure only direct observations contribute to the spectral content in the window. Subsequently, we estimate the data coverage of every window and discard windows with less than 80% data coverage to ensure that the recovered CPD estimates are not dominated by interpolation effects.

It is common for spectral methods that the study area is subdivided into windows which have a large overlap between them (Audet & Gosselin, 2019; Blakely, 1988; Bouligand et al., 2009; Idárraga-García & Vargas, 2018; Leseane et al., 2015; Okubo et al., 1985). The overlap increases the number of depths estimates and is expected to increase resolution up to a point, which allows the investigation of lateral variations in CPD through the study area. The overlapping windows also allow smoothing of the more closely spaced CPD estimates (Section S2 in Supporting Information S1). In this study we use a step size of 20 km between the analytic windows, which results in a large overlap between the windows. A Hanning taper is applied to the windowed subgrid in the space domain to remove edge discrepancies. No further modification, corrections or filters have been applied to the magnetic grid and power spectrum in line with recommendations from previous authors (Audet & Gosselin, 2019; Núñez Demarco et al., 2020; Ravat et al., 2007).

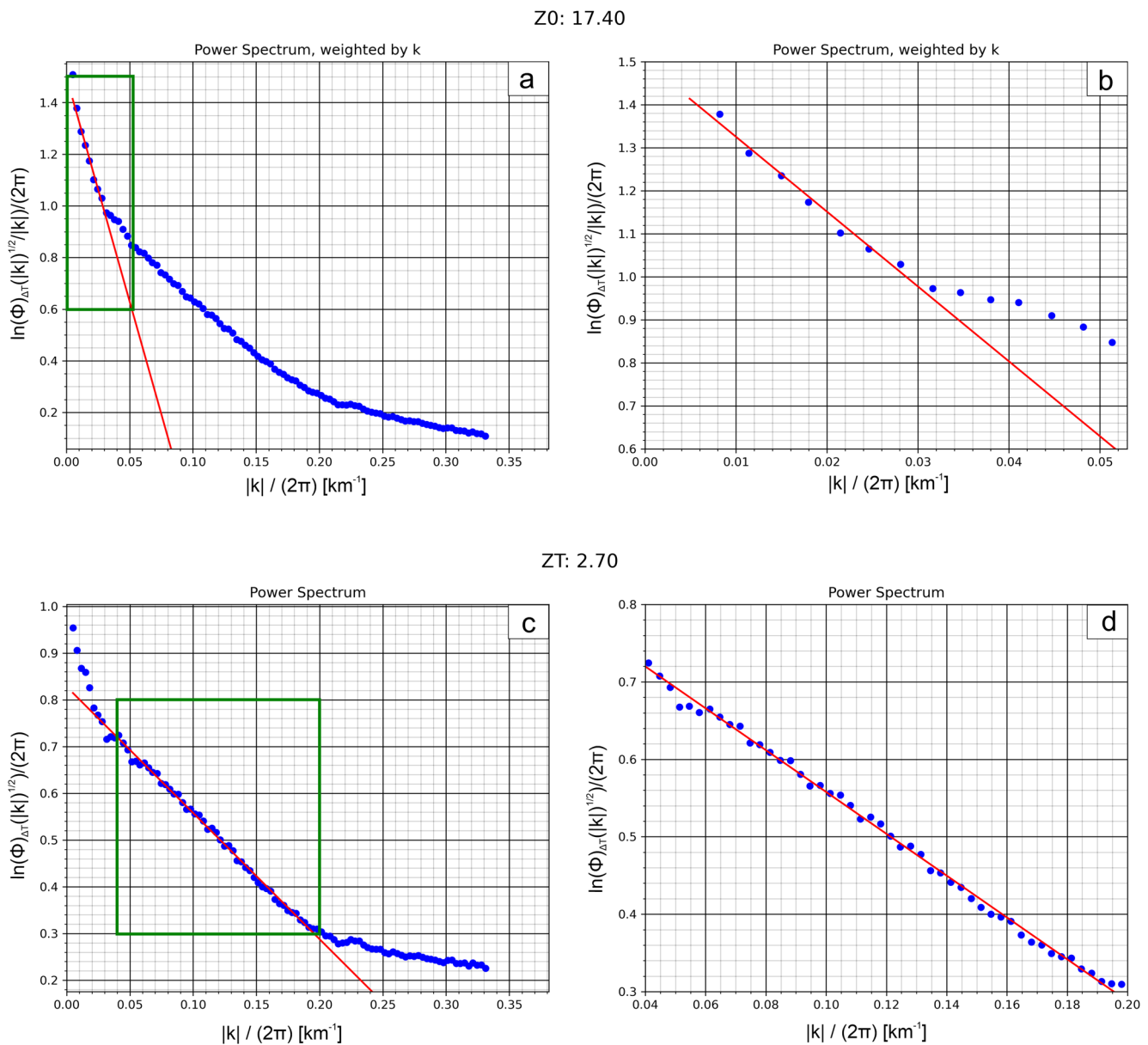


Figure 4. Power spectrum from window 645, centroid location and extension of the window is given in Figure 3b (a) Power spectrum weighted by k to estimate Z_0 . Red line represents the fitted line through the low wavenumber part of the power spectrum. Green rectangle illustrates zoom in range for (b). (b) Zoomed in power spectrum weighted by k (c) Power spectrum to estimate Z_t . Red line represents the fitted line through the high wavenumber part of the power spectrum. Green rectangle illustrates zoom in range for (d). (d) Zoomed in power spectrum.

Applying this approach, with a threshold of 80% data coverage, we obtain 2,161 valid windows for a window size of 200 km, 1,933 windows for a window size of 300 km and 1,685 windows for the window size of 400 km. Our approach is limited to regions with relatively good airborne data coverage and therefore cannot be applied to the entire Antarctic continent.

A fixed wavenumber range is used to estimate the CPD in each window. Z_0 is calculated in the wavenumber range 0.006–0.033 $|k|/2\pi$ (167–30 km wavelength) and Z_t is calculated in range 0.04–0.2 $|k|/2\pi$ (25–25 km wavelength) respectively. The ideal wavenumber range for Z_0 is defined as the first linear segment after the spectral peak in the low wavenumber part of the power spectrum, while the ideal range for Z_t is defined as the second linear segment in the power spectrum. The linear regression (Figure 4) to estimate Z_t and Z_0 is carried out using the function *curve fit* from the python library SciPy learn (Virtanen et al., 2020). The uncertainty of the fitted slope

is calculated by estimating the standard deviations from the covariance matrix by taking the square root of the diagonals (Equation 6) and propagating the uncertainty (Equation 7).

$$\sigma_{\text{slope}} = \sqrt{Cov_{\text{diag}}} \quad (7)$$

$$\sigma_{\text{CDP}} = \sqrt{\sigma_{\text{slope}[z_i]}^2 + 2\left(\sigma_{\text{slope}[z_0]}^2\right)} \quad (8)$$

We note that the estimated uncertainty is a formal error, which describes how well the linear regression fits the radially averaged power for the predefined wavenumber range. The absolute uncertainty of the CPD estimation may surpass this formal error (see Section 5.2).

CPD estimations, which are an approximation for the 580°C Curie isotherm can be used as a proxy for GHF. Where CPDs are shallow a higher GHF is expected and vice versa. A first order approximation of GHF from CPD estimates can be inferred from Fourier's Law (Equation 8) (Núñez Demarco et al., 2020; Turcotte & Schubert, 2002).

$$Q = -K \frac{\partial T}{\partial z} = -K \frac{T_c - T_{\text{surface}}}{Z_b} \quad (9)$$

where Q is the heat flux at the bedrock interface, T_c is the Curie temperature (580°C), T_{surface} is the surface temperature, Z_b is the CPD and K is the thermal conductivity. Here, a thermal conductivity of 2.5 W/mK is used, which is the average thermal conductivity of igneous rocks (Clauser & Huenges, 1995; Goes et al., 2020; Hasterok et al., 2018; Jennings et al., 2019). Temperature at the bedrock surface (T_{surface}) is set to 0°C in line with previous spectral analysis studies in Antarctica (Dziadek et al., 2021; Martos et al., 2017). Assuming 0°C at the bedrock interface is sufficient since most of the bottom of the ice sheet has been calculated to be at the pressure melting point around -2°C with a variation of a few °C, which results in a “wet base” of the icesheet (Pattyn, 2010). This assumption breaks for areas with dry base ice sheet and areas with no ice cover. Over most of this region annual mean surface temperatures are -20 to -50°C (Wang & Hou, 2009). We performed a sensitivity test for the dry base ice sheet and ice-free scenario assuming an annual surface temperature of -30°C (Figure S3 in Supporting Information S1). This effect would bias averaged heat flow by 4 mW/m², which is considerably less than the overall uncertainty estimated for the GHF (Figures 6d–6f). Therefore, this effect is considered negligible. Using an ice surface temperature is also problematic due to the potential for melting/freezing in the ice as well as fluid flow. Equation 8 is a strong simplification of the real world since it neglects spatial variation of thermal conductivity caused by for example, geology as well as any heat production in the area due to for example, radiogenic heat production in crustal rocks. Those parameters are strongly influenced by the composition of the present crustal rocks, which are poorly constrained in Antarctica due to the thick overlaying ice sheet (Burton-Johnson et al., 2020). (Martos et al., 2017) accounted for crustal heat production by using a constant value for the entire Antarctic continent, which does not help the conversation on spatial GHF variation caused by heterogeneity within the crust.

4. Results

The CPD estimates range between 15 and 35 km (Figures 5a–5c). A low CPD value indicates a shallow Curie isotherm of 580°C and therefore implies a higher heat flow and vice versa. A prominent shallow CPD province is present beneath the TAM between -78° and -72° latitude for all three window size configurations. In the area of the RG a linear shallow feature is visible in the 200 and 300 km windows (Figures 5a and 5b) but is much subdued in the 400 km window (Figure 5c). Another linear feature is observed in the Central Basin (Figures 5a and 5b).

Again, this feature is subdued in the 400 km window (Figure 5c). West of the CB, deeper CPD values are observed, indicating an overall colder thermal structure. CPD estimates from the 200 km window have a higher frequency in their spatial pattern compared to window size configurations of 300 and 400 km (Figures 5a–5c). With increasing window size, the range of recovered CPD decreases, while the mean depths become deeper (Figures 5a–5c and 7a–7c). Moreover, the estimated uncertainties decrease with increasing window size (Figures 5a–5f). Linear transformation of CPD to GHF maps (see Equation 8) yielded estimates ranging from 38 to 110 mW/m². The spatial patterns in the GHF maps (Figures 6a–6c) are identical to those observed in the CPD map (Figures 6a–6c)

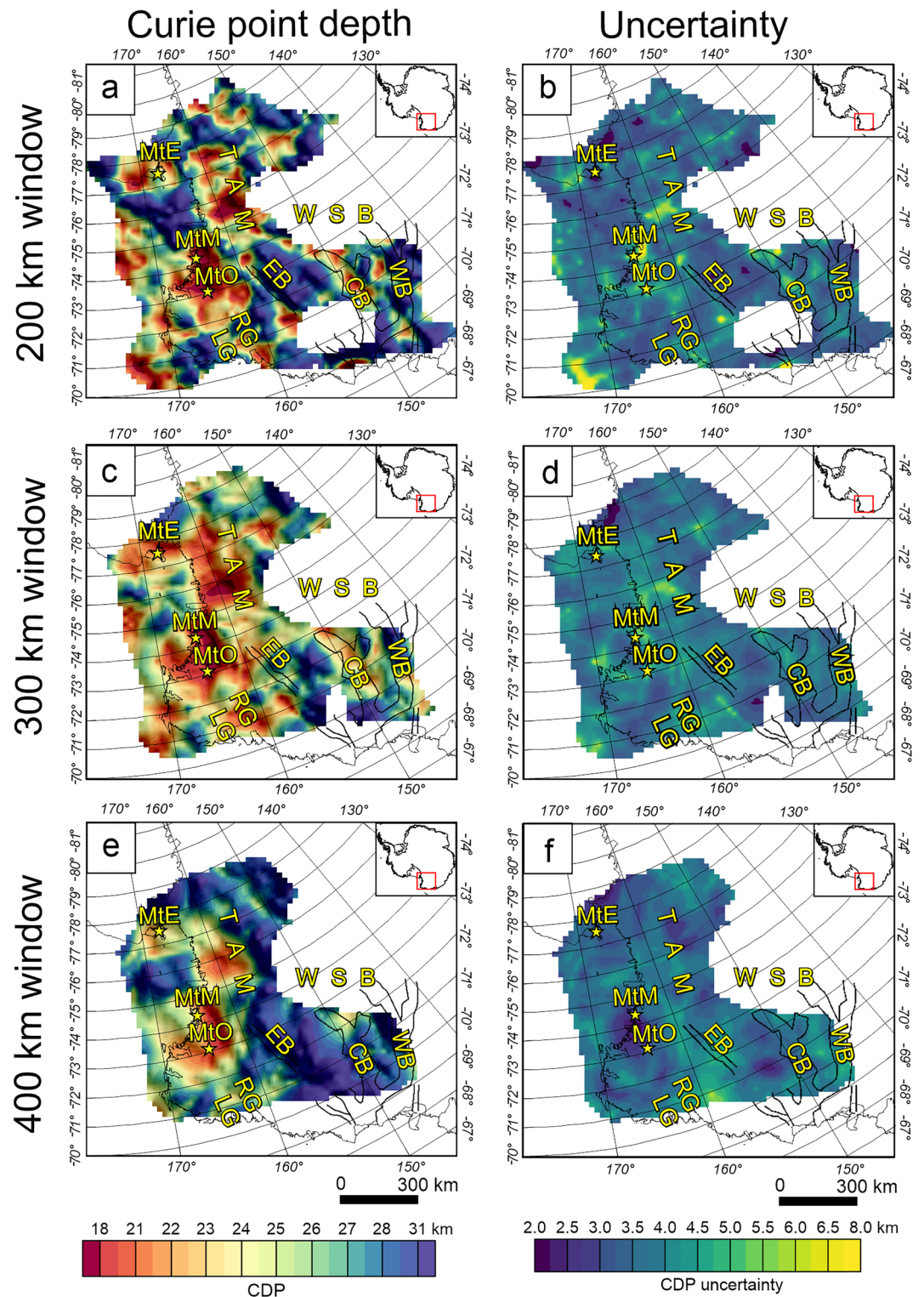


Figure 5. Left column gives Curie Point Depth (CPD) estimates for different window sizes. Right column illustrates the corresponding uncertainty. (a) CPD based on a 200 by 200 km window. (b) Uncertainty for CPD estimates based on a 200 by 200 km window. (c) CPD estimates obtained with a 300 by 300 km window. (d) Uncertainty for CPD estimates obtained with a 300 by 300 km window. (e) Calculated CPD with a 400 by 400 km window. (f) Uncertainty for CPD estimates with a window size of 400 by 400 km. LG: Lillie Graben; RG: Rennick Graben; EB: Eastern Basin; CB: Central Basin; WB: Western Basin; WSB: Wilkes Subglacial Basin; TAM: Transantarctic Mountains; MtE: Mount Erebus; MtM: Mount Melbourne; MtO: Mount Overlord. Identical colormap used for (a, c, and e) and (b, d, and f).

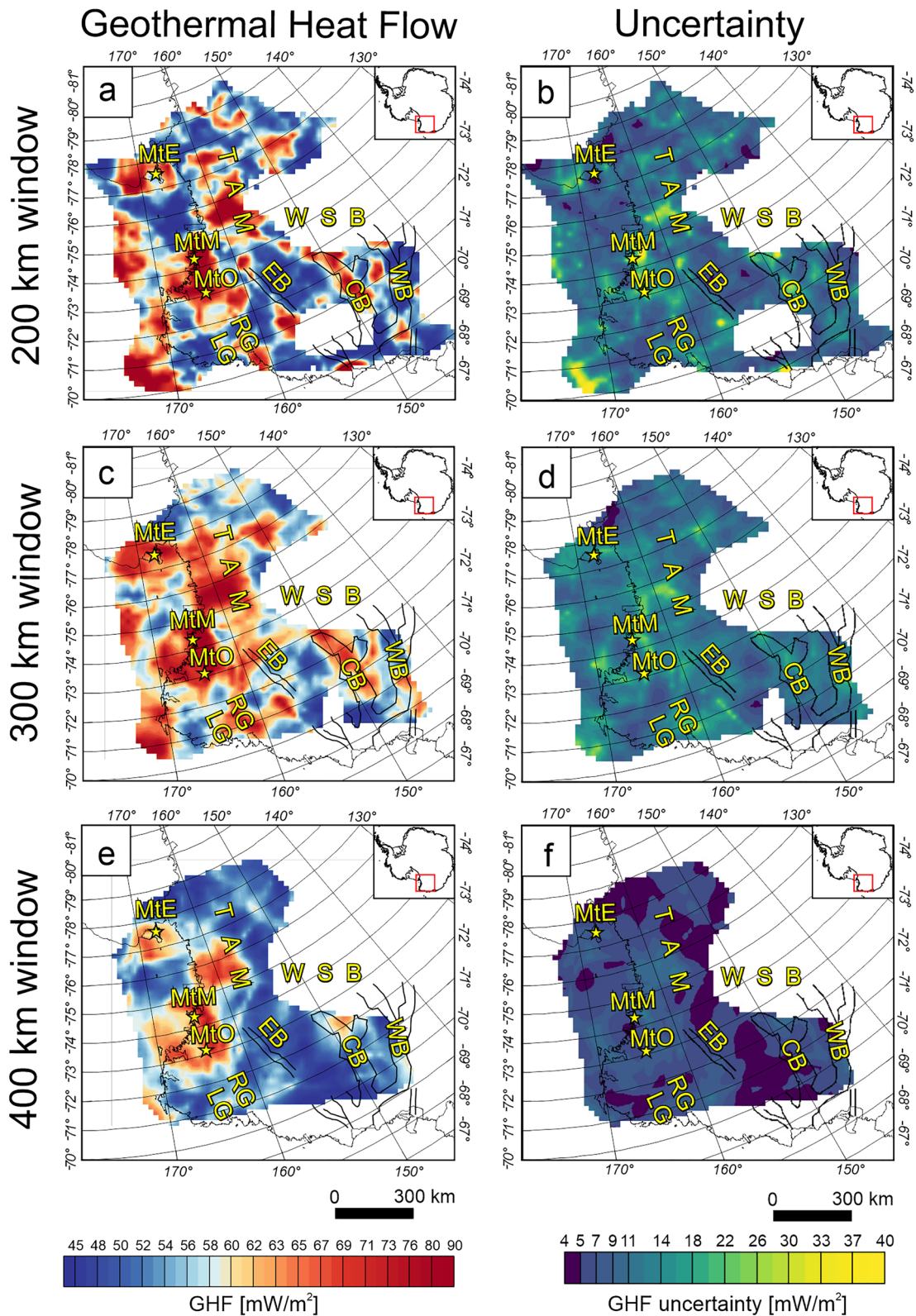


Figure 6.

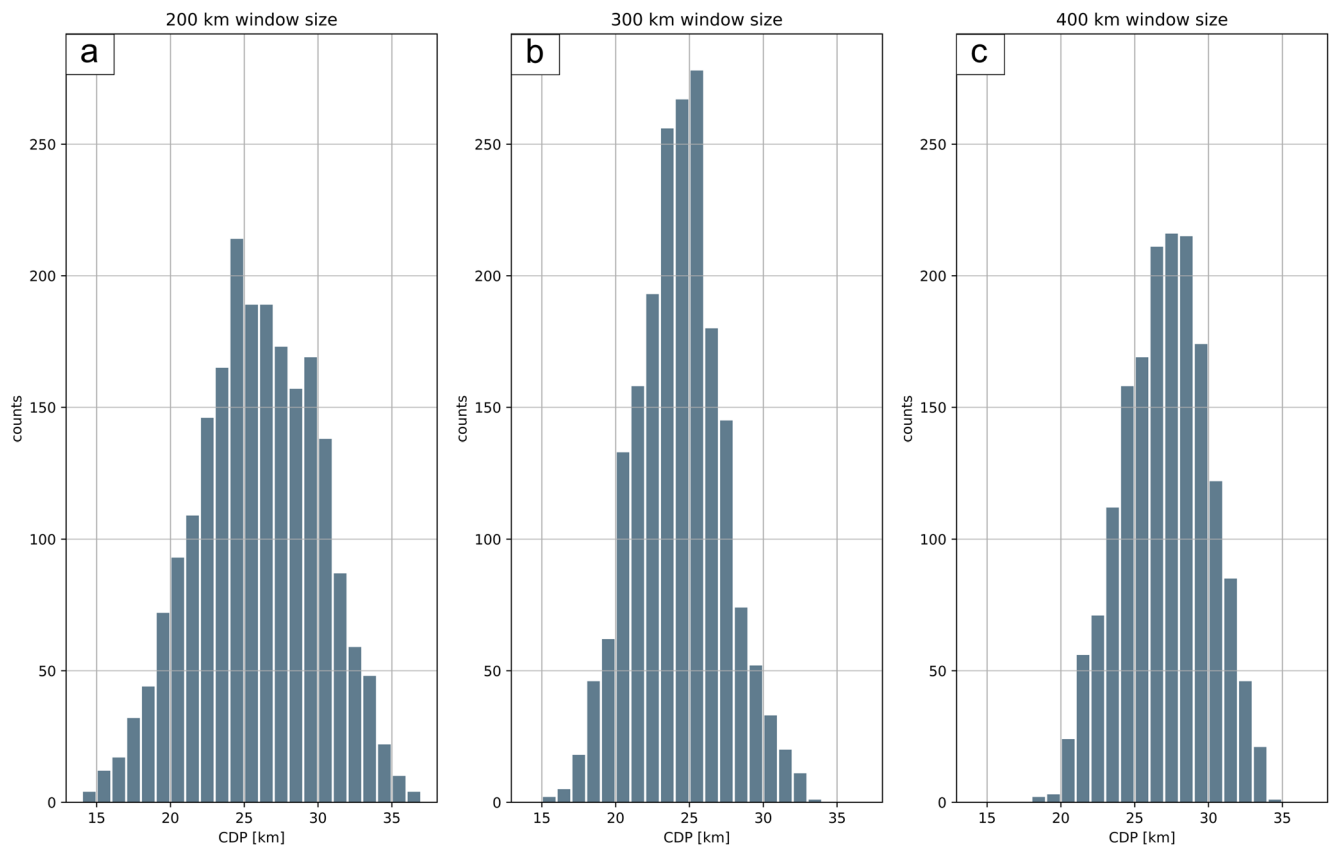


Figure 7. Histogram of recovered Curie Point Depth (CPD) depth for different window sizes with a bin size of 1 km. (a) CPD estimates recovered from 200 by 200 km windows. (b) CPD estimates obtained using 300 by 300 km windows. (c) Recovered CPD based on 400 by 400 km windows.

due to the linear relationship between both maps. Again, the range of GHF values decreases with increasing window size while the error decreases also with increasing window size (Figures 6a–6f).

5. Discussion

Results recovered from a window size of 300 and 400 km are preferred for multiple reasons: First, the recommendation for an optimal window size is 5–10 times the recovered CPD (Ravat et al., 2007) (see Section 3.1). The largest portion of recovered CPD across all window sizes is between 25 and 30 km (Figure 7). Aiming for a window size which is 10 times the recovered CPD the preferred windows size must be larger than 250 km and thus the 300 km window size in our study is best suited to satisfy this recommendation. In addition, a window size of 300 km recovers a larger number of valid CPD estimates for the study area in comparison to the 400 km window size (Figures 7a–7c).

The estimated error for the CPD estimates based on the fitting of the radially averaged power spectrum decreases with increasing window size (Figures 5d–5f), which points in the direction of missing low wavenumber content in the 200 km window, while larger window sizes are stabilized due to capturing a wider bandwidth. Moreover, high frequency of spatial variation in the CPD is observed in the 200 km window (Figure 5a), while CPD from a larger window size (Figures 5b and 5c) shows less spatial variation. A large change between the results obtained from a 200 to 300 km window is observed, although many key features persist. A much smaller change is observed

Figure 6. Left column gives geothermal heat flow (GHF) estimates for different window sizes. Left column illustrates the corresponding uncertainty. (a) GHF based on a 200 by 200 km window. (b) Uncertainty for GHF estimates based on a 200 by 200 km window. (c) GHF estimates obtained with a 300 by 300 km window. (d) Uncertainty for GHF estimates obtained with a 300 by 300 km window. (e) Calculated GHF with a 400 by 400 km window. (f) Uncertainty based on GHF estimates with a window size of 400 by 400 km. LG: Lillie Graben; RG: Rennick Graben; EB: Eastern Basin, CB: Central Basin; WB: Western Basin; WSB: Wilkes Subglacial Basin; TAM: Transantarctic Mountains; MtE: Mount Erebus; MtM: Mount Melbourne; MtO: Mount Overlord. Identical colormap used for (a, c, and e) and (b, d, and f).

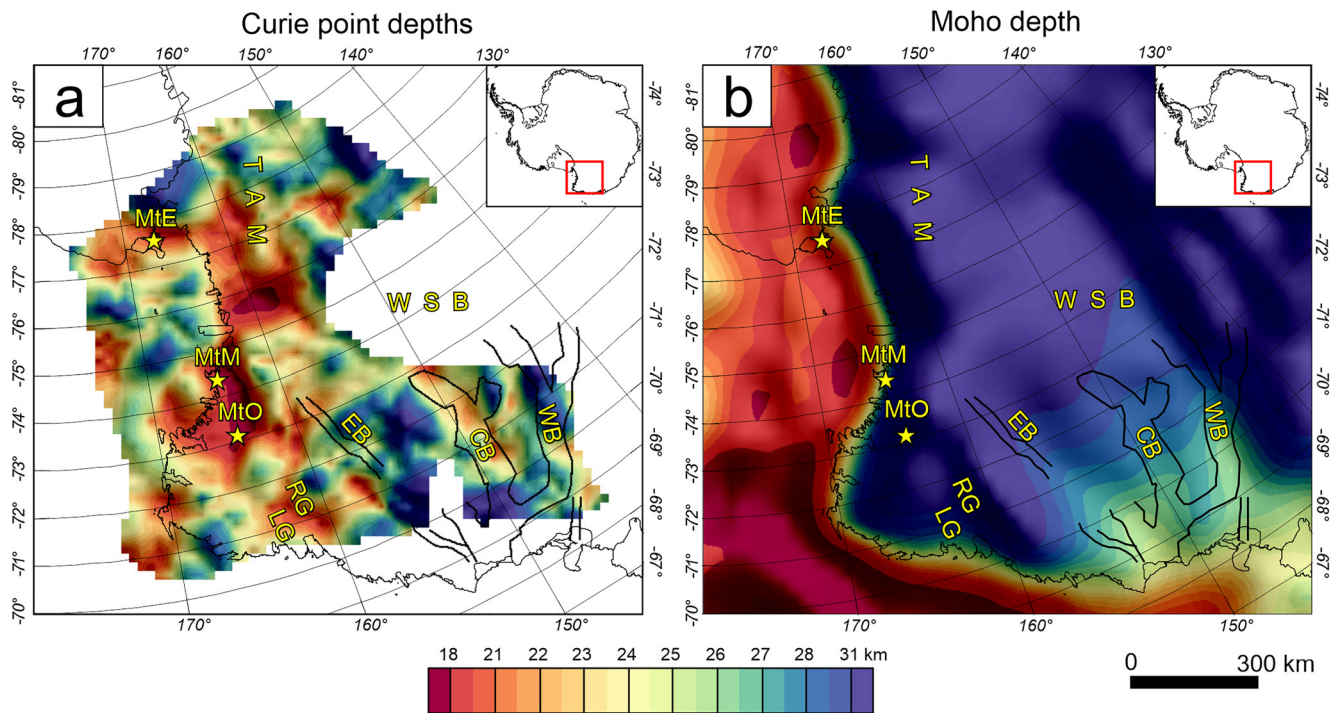


Figure 8. (a) Curie Point Depth estimates recovered with a 300 km window size. (b) Moho depth map inferred from satellite gravity inversion (Pappa et al., 2019). Yellow stars indicate the location of recent active volcanoes. LG: Lillie Graben; RG: Rennick Graben; EB: Eastern Basin; CB: Central Basin; WB: Western Basin; WSB: Wilkes Subglacial Basin; TAM: Transantarctic Mountains; MtE: Mount Erebus; MtM: Mount Melbourne; MtO: Mount Overlord. Identical colormap used for (a and b)

between the result obtained from a 300 and 400 km window, suggesting the recovered CPD values stabilize for windows larger than 200 km. Lastly, CPD resulting from a 300 km window recovered spatial patterns, which are consistent with geological and topographic features like the RG and the CB. Based on the arguments above we prefer results obtained from a window size of 300 km.

CPD estimates are the result of the average Curie depth within the analyzing window, although a strong depth variation within the window may bias the estimation to deeper or shallower values. Moho depth maps are a good control mechanism since Curie depths deeper than the Moho interface would imply that the upper mantle is magnetic, which is not typically assumed (e.g., (Wasilewski et al., 1979)), although this possibility has been suggested (Ferré et al., 2014). CPD estimations of this study are above the Moho interface onshore with a few exceptions near the edge of the magnetic data coverage (Figure 8). CPD estimate offshore in the Ross Sea show isolated areas with deeper CPD estimates compared to the Moho map from Pappa et al. (2019).

Recovered CPDs ranging from 15 to 35 km are not unusual compared to different regions elsewhere on the globe. CPDs for the mid-Norwegian margin in the area of the Trøndelag Platform and Vøring Basin are reported to range from 18 to 20 km at the coast, around 12 km at the ocean continent transition zone and beneath the oceanic plate to be in the order of about 9 km (Ebbing et al., 2009) CPDs beneath the British Isles are reported to range from 15 to 45 km (Mather & Fulla, 2019). CPDs in southern Africa are reported to range from 8 to 15 km along the Okavango Rift zone in Botswana and up to 50 km in the Kaapvaal Craton (Sobh et al., 2021). Curie depths substantially shallower are reported for the West Antarctic Rift system, reaching depths shallower than 10 km and up to extreme values of 4.8 km (Dziadek et al., 2021). Such extreme shallow CPD values are highly unlikely in the cratonic region of East Antarctica.

5.1. Uncertainty of CPD and GHF Estimation

Uncertainty arising from fitting the slope of the predefined wavenumber range varies between 2 and 8 km throughout the study area (Figures 5d–5f), which translate to an uncertainty of 2.9–48.8 mW/m² for the GHF estimation. Uncertainty associated with choosing inappropriate size and range of the wavenumbers to calculate

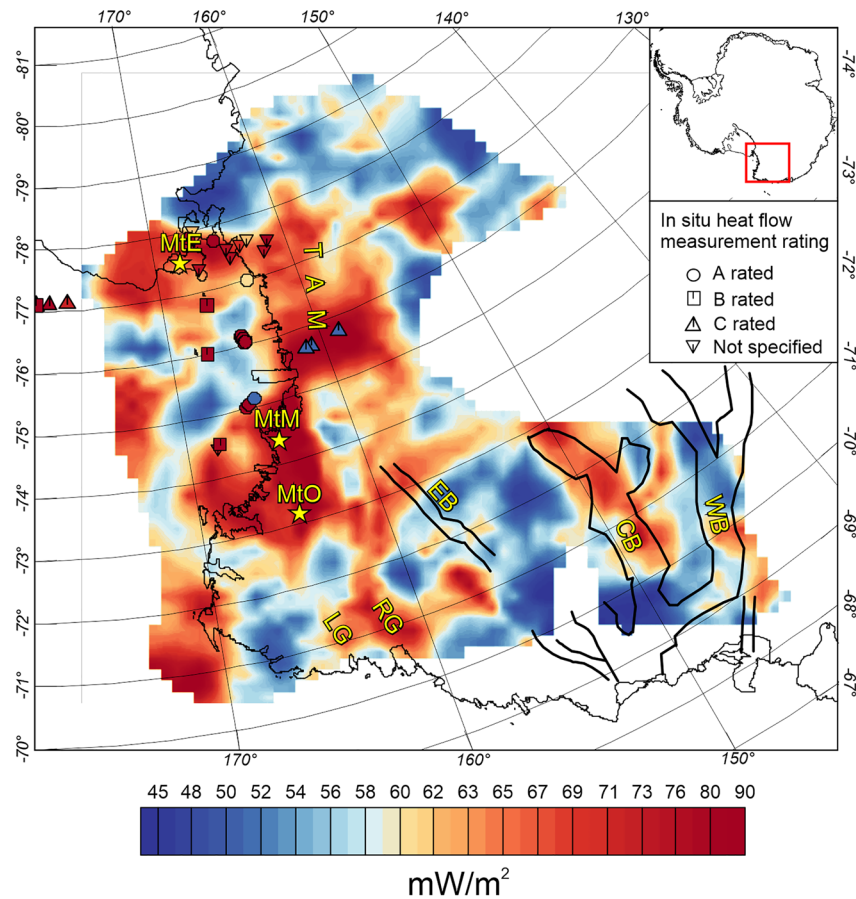


Figure 9. In situ geothermal heat flow (GHF) measurements (Lucazeau, 2019) superimposed on GHF estimates recovered based on an analytic window with a window size of 300 km. Circles represent A rated GHF measurements, Boxes represent B rated GHF measurements, regular triangles represent C rated GHF measurements and inverted triangles represent Z rated (not specified) rated GHF measurements. Yellow stars indicate the location of recent active volcanoes. LG: Lillie Graben; RG: Rennick Graben; EB: Eastern Basin; CB: Central Basin; WB: Western Basin; WSB: Wilkes Subglacial Basin; TAM: Transantarctic Mountains; MtE: Mount Erebus; MtM: Mount Melbourne; MtO: Mount Overlord. Identical colormap is applied to the GHF map and the measured heat flow values. Identical colormap used for Figures 10a–10f.

Z_0 and Z_i can lead to significantly different CPD results of the order of multiple km (Section S4 in Supporting Information S1). Uncertainty from the chosen window size is in the order of a few km (Figures 5 and 7). With increasing window size, the average recovered depths increase, while fewer extreme CPD values are recovered (Figures 5, Figure 7). Moreover, the composition of the magnetic material itself induces uncertainty since the Curie temperature is not a universal 580°C for all minerals (Blakely, 1988; Haggerty, 1978; Núñez Demarco et al., 2020). However, the effect of the mineral composition is almost impossible to quantify. Lastly, the linear transformation of CPD to GHF (Equation 8) does not consider heat production within the crust and assumes a constant thermal conductivity, which is a strong simplification of the crustal properties.

It is important to consider these effects when using absolute values of GHF estimates derived from bottom of the magnetic layer methods. However, many of the uncertainties discussed above relate to the absolute value of the CPD across the study. This method therefore provides a robust tool for imaging relative variation in CPD, but absolute values should be used with more caution.

5.2. Comparison to In-Situ GHF Measurements and Previous GHF Models

The global GHF catalog (Lucazeau, 2019) reports a few in situ measurements for the study area (Figure 9). These measurements use different techniques and equipment. Measurements in our study area have been conducted from boreholes, sediment and ice probes (Lucazeau, 2019). The measurements in the database are rated from A

to C based on the variation of heat with depths and Z for not specified. A rated GHF measurements (circles in Figure 9) are very sparse in the area. The three southernmost (longitude from 163° to 165°, latitude from -77° to -77.7°) A rated measurements are conducted in boreholes and consistent with our GHF estimates. A rated measurements offshore are aligned at the edge of a high heat flow pattern. However, the negative heat flow pattern offshore arises from CPD estimates, which are below the Moho interface and therefore are less trustworthy as discussed in Section 5. B and Z rated GHF measurements are overall consistent with our GHF estimates. C rated measurements onshore (triangles Figure 9) are in strong disagreement with our findings. Previous GHF models based on machine learning and multi statistical similarity analysis (Lösing & Ebbing, 2021; Stål et al., 2021) use in situ measurements in their approach. However (Stål et al., 2021), only used A rated GHF measurements, while (Lösing & Ebbing, 2021) did not discriminate the measurements. We categorize the three borehole measurements taken beneath the McMurdo ice Shelf (longitude from 163° to 165°, latitude from -77° to -77.7°) to be the most trustworthy and are more cautious in regard to measurements obtained using sediment and ice probes.

Difference-maps (Figure 10) between the GHF estimates based on a 300 by 300 km window to previous studies (Figure 2) show moderate differences in the order of ± 20 mW/m² between most models with isolated areas with stronger disagreement ± 50 mW/m² and more. All models predict a lower GHF beneath the southern TAM and a higher heat flow offshore. The seismic derived GHF estimates (An et al., 2015; Shen et al., 2020) show the least disagreement together with the statistically derived model from Stål et al. (2021) to GHF estimates in this study.

Those three models predict GHF values in the same order of magnitude with stronger disagreements in the RG, CB and southern TAM. The GHF model derived from magnetically inferred CPD from Martos et al. (2017) shows a strong disagreement at the divide to West Antarctica and a moderate disagreement in East Antarctica. The strong disagreement might be due to the fact that the Martos et al. (2017) study applied different wavenumber ranges to the power spectrum to estimate the CPD for windows in West and East Antarctica, which systematically gives shallower CPD for West Antarctica and consequently results in higher heat flow. GHF prediction based on a machine learning approach by Lösing and Ebbing (2021) shows strong disagreement onshore beneath the southern TAM and offshore in the Ross Sea. The much lower GHF predictions in the Lösing and Ebbing (2021) model onshore beneath the TAM might be related to incorporating the three C rated GHF in situ measurements from the global GHF catalog (Lucazeau, 2019). The large difference in the Ross Sea to the Lösing and Ebbing (2021) model is located where our CPD estimates exceed the Moho depth and therefore are less trustworthy. Figure 10 illustrates that our results predict higher heat flow beneath the TAM extending westwards, while high heat flow values in previous models are limited to the region closer to the coastline.

5.3. Geological Origins and Implications of Geothermal Anomalies

Curie Point Depth estimation and GHF predictions derived from them reveal elevated heat flow beneath the northern TAM. Recently active volcanoes in the study area are: Mount Erebus, which is the southernmost active volcano on Earth (Sims et al., 2021), Mount Melbourne, a quiescent volcano, which is believed to have the potential to produce major explosive events (Gambino et al., 2021), and Mount Overlord, which was active during the Eocene (Perinelli et al., 2017). Those recently active volcanoes are consistent with thermal anomaly pattern of this study since each volcano is centrally located in areas of elevated heat flow (Figure 9).

The high in heat flow in the TAM region is in line with the idea of warmer West Antarctic mantle beneath the TAM providing thermal support for the mountain range as proposed by Hansen et al. (2016) and the low velocity mantle imaged by recent seismic tomography models (Lloyd et al., 2020; Wiens et al., 2021).

A linear high heat flow anomaly is observed in the RG. This high heat flow pattern leaks into the Lillie Graben. The opening of the RG was previously linked to mid Cretaceous (~100 Ma) rifting and interpreted as a failed rift arm (Fleming et al., 1993). This idea is challenged by fission track data, which indicates that the RG formed due to tectonic denudation (up to 5 km) combined with strike-slip deformation (Rossetti et al., 2003). A receiver function profile perpendicular to the RGn (Station BI01–BI03) indicates shallow crustal thickness of 24 km (Agostinetti et al., 2004). Both mechanisms, mid Cretaceous rifting and large amount of denudation, could explain elevated heat flow in the RG as seen in our results. Alternatively, small crustal thicknesses accompanied by a thin lithosphere can cause an elevation in heat flow. However, the thin crust imaged by receiver functions is not limited to the RG and would cause broader high heat flow patterns in contrast to the narrow heat flow pattern imaged by our results.

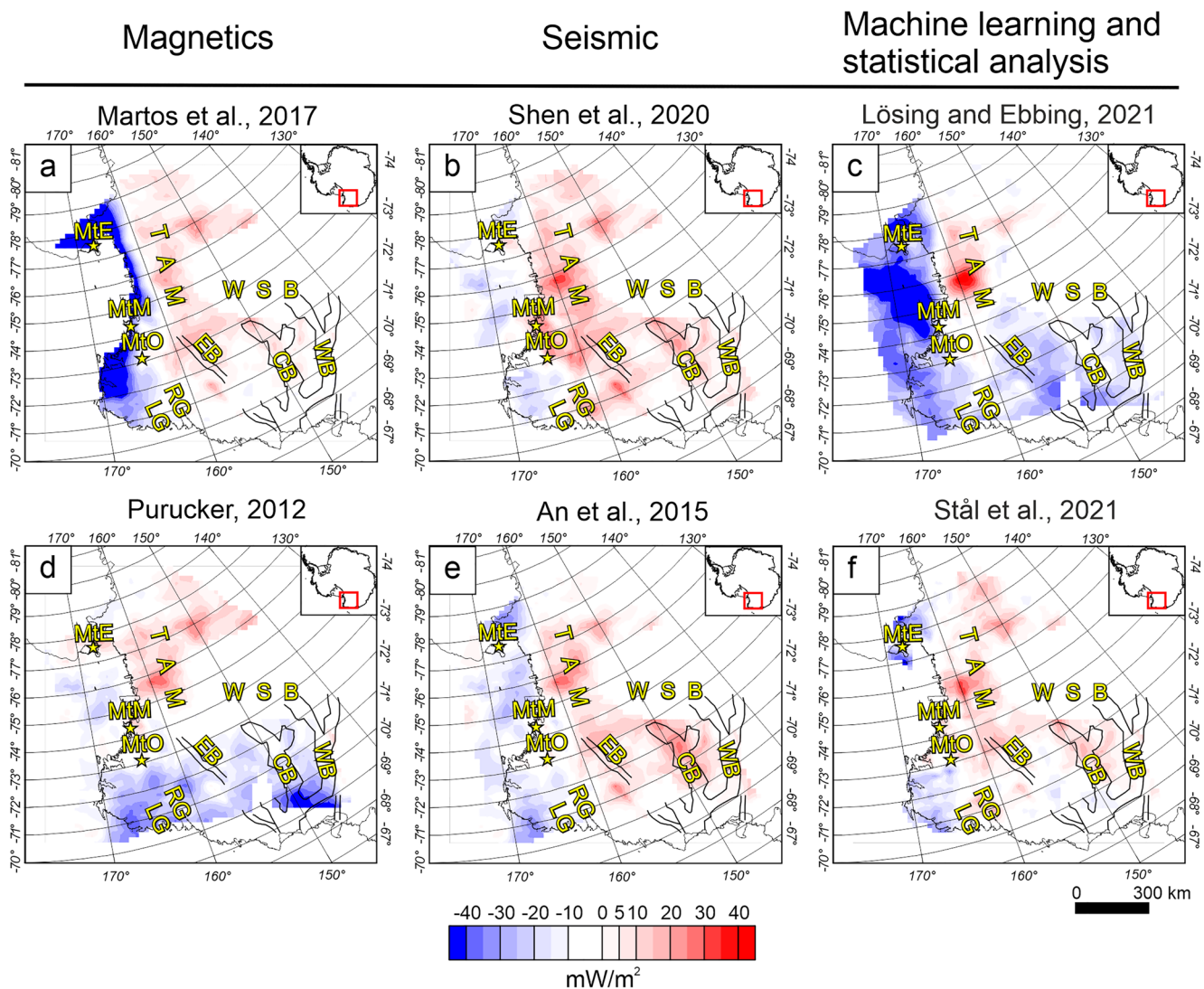


Figure 10. Difference-maps between geothermal heat flow (GHF) estimates of this study obtained with a window size of 300 by 300 km and existing continent wide GHF models shown in Figure 2. Blue colors show lower GHF values in GHF estimates in this study, while red colors indicate higher GHF estimates in this study. (a) Difference in estimated GHF values compared to (Martos et al., 2017) (b) Difference in estimated GHF values compared to Shen et al. (2020) (c) Difference in estimated GHF values compared to Lösing and Ebbing (2021). (d) Difference in estimated GHF values compared to Purucker (2013) an update of Fox Maule et al. (2005). (e) Difference in estimated GHF values compared to An et al. (2015), and (f) Difference in estimated GHF values compared to Stål et al. (2021). LG: Lillie Graben; RG: Rennick Graben; EB: Eastern Basin; CB: Central Basin; WB: Western Basin; WSB: Wilkes Subglacial Basin; TAM: Transantarctic Mountains; MtE: Mount Erebus; MtM: Mount Melbourne; MtO: Mount Overlord.

Another linear geothermal feature is imaged in the Central Basin (Figure 6b). Competing models of the WSB origin have been proposed in the past, including continental rifting (Steed, 1983), which was partially supported by airborne geophysical data (Ferraccioli et al., 2001). However, interpretation of recent aerogeophysical data suggested a rifting origin of the CBn is very unlikely (Ferraccioli, Armadillo, Jordan, et al., 2009; Jordan et al., 2013). Alternative models include flexural down-warp of the WSB in response to Cenozoic rift-flank uplift of the TAM caused by the neighboring Ross Sea Rift (Stern and ten Brink, 1989; ten Brink et al., 1997). Similarly, a recent model proposes the WSB developed as a result of flexural processes coupled with deep glacial erosion (Paxman et al., 2019). Both mechanisms, continental Cenozoic rifting, even though unlikely, and large-scale erosion, can cause elevated heat flow and might be connected to the high heat flow pattern observed in the CB. The similarity in amplitude and linear pattern of heat flow in the RG and the CB could be an indicator of a similar evolution mechanism. In the broader WSB area, except for the RG and CB the CPD and GHF maps show overall deeper and lower values, respectively, and therefore indicate a much colder thermal structure.

The CPD and consequently GHF maps from this study have a higher spatial resolution than previous continental scale GHF estimates inferred from magnetic data (Figures 2a and 2d), due to a combination of smaller distance between evaluated windows (20 km) and using only high-resolution airborne data without substituting satellite measurements. Consequently, the spatial coverage of our approach is strongly limited to the region with a dense coverage of airborne measurements, however, where results are obtained, we believe them to be more robust.

6. Conclusion and Future Work

We present new CPD and GHF maps for the northern TAM and WSB area. Our spectral analysis of magnetic data provides a significant improvement over prior GHF maps of the region. We image elevated heat flow beneath the TAM, which extends further west than previously mapped. We also resolve elevated heat flow features in the RG and CB that have not been imaged before. However, the overall spatial coverage of this analysis is limited by the extent of airborne surveys with close flight line spacing. Filling data gaps with satellite magnetic data, as previous studies in Antarctica have done (Dziadek et al., 2021; Martos et al., 2017) is not an effective solution due to the limited range of wavelengths it provides for the analytic window (Pappa & Ebbing, 2021). Previous Antarctic CPD studies have failed to report the centroid location of the analyzed window, the power spectrum of the analyzed window, or the intercept and slope values for the linear regression, which makes it impossible to directly reproduce them. We report for the first time all those parameters for a CPD study in Antarctica, which makes this study fully reproducible. We encourage CPD studies in Antarctica to follow the guidance for reproducibility by Núñez Demarco et al. (2020).

The shallow Curie depth values estimated beneath Northern Victoria Land and the TAM provide independent evidence favoring the hypothesis that warmer West Antarctica mantle provides thermal support for this part of the TAM, as imaged by seismological studies (Hansen et al., 2016; Lloyd et al., 2020; Wiens et al., 2021). High GHF values beneath the northern TAM and West Antarctica are also consistent with the presence of recently active volcanoes including Mount Erebus, Mount Melbourne and Mount Overlord.

Our GHF maps are a linear transformation from the CPD estimates and provide a good estimate of relative variations of the thermal structure. However, due to the high uncertainty of CPD estimates (Section 5.2) and the simplified linear transformation to GHF (Equation 8), absolute GHF values derived from spectral methods should be used with caution.

Despite the many assumptions and lack of onshore heat flow control data, the Curie depth and GHF results show convincing coherence and highlight interesting comparisons with known geological features. The approach of using exclusively high-resolution airborne data should be repeated in other areas of Antarctica with suitable magnetic data coverage to obtain relative variation in CPD. Future studies examining variation of β values could provide a meaningful tool for revealing subglacial geology in the area. Another, potentially more practical way could be, to combine magnetic data with gravity data in a mutual information inversion framework to constrain subglacial geology and crustal boundaries like the depth to the bottom of magnetic sources (Lösing et al., 2022).

Data Availability Statement

CPD and GHF estimates from this study are available through the Polar Data Centre. In addition, power spectrum for each window and parameter of the linear regression are made publicly available for the purpose of reproducibility (<https://doi.org/10.5285/B8DCBAA9-3AC0-42BD-95A5-6B5961CBCB7E>). BedMachine Antarctica version 2 (Morlighem et al., 2020) is freely available at <https://nsidc.org/data/NSIDC-0756/versions/2>, ADMAP-2 magnetic data (Golynsky et al., 2018) is freely available at <https://doi.pangaea.de/10.1594/PANGAEA.892724>, The LCS-1 data (Olsen et al., 2017) can be freely accessed at <http://www.spacecenter.dk/files/magnetic-models/LCS-1/>. GHF model from Shen et al. (2020) is available at <https://drive.google.com/file/d/1Fz7dAHTzPnlytuyRNctk6tAugCAjizR/view>. GHF model from Lösing and Ebbing (2021) is available from <https://doi.pangaea.de/10.1594/PANGAEA.930237?format=html#download>. GHF model from Stål et al. (2021) is available at: <https://doi.pangaea.de/10.1594/PANGAEA.924857>. GHF model from Martos et al. (2017) is available at <https://doi.pangaea.de/10.1594/PANGAEA.882503>. GHF model from Purucker an update of Fox Maule et al. (2005) is available at http://websrv.cs.umt.edu/isis/images/c/c8/Antarctica_heat_flux_5km.nc. Heat flux map from An et al. (2015) is available at: <http://www.seismolab.org/model/antarctica/lithosphere/AN1-CTD.tar>.

gz. Python code in form of a Jupyter notebook to reproduce the result of this study is available at: <https://zenodo.org/badge/latestdoi/524783702>.

Acknowledgments

Funding for this research was provided by NERC through a SENSE CDT studentship (NE/T00939X/1). ML acknowledges additional funding through the Gray-Milne Travel Bursary provided by the British Geophysical Association, Covid-19 Support Fund awarded by the British Geophysical Association and the Small IT Grant awarded by the School of GeoSciences, The University of Edinburgh. ML acknowledges Dr. Fausto Ferraccioli for proposing the PhD project, which this research is part of, through the SENSE CDT. The authors thank the developers of open scientific software products which were utilized in this study: Pycurious (Mather & Delhaye, 2019), SciPy learn (Virtanen et al., 2020), NumPy (Harris et al., 2020), Matplotlib (Hunter, 2007), Pandas (McKinney, 2010), Jupyter notebook (Kluyver et al., 2016) as well as the developer of the commercial software Geosoft, especially the plug-in “Compudrape” and their publisher Seequent.

References

- Agostinetti, N. P., Amato, A., Cattaneo, M., & Di Bona, M. (2004). Crustal structure of Northern Victoria Land from receiver function analysis. *Terra Antarctica*, 11(1), 5–14.
- An, M., Wiens, D. A., Zhao, Y., Feng, M., Nyblade, A., Kanao, M., et al. (2015). Temperature, lithosphere-asthenosphere boundary, and heat flux beneath the Antarctic Plate inferred from seismic velocities. *Journal of Geophysical Research: Solid Earth*, 120(12), 8720–8742. <https://doi.org/10.1002/2015JB011917>
- Audet, P., & Gosselin, J. M. (2019). Curie depth estimation from magnetic anomaly data: A re-assessment using multitaper spectral analysis and Bayesian inference. *Geophysical Journal International*, 218(1), 494–507. <https://doi.org/10.1093/gji/ggz166>
- Bansal, A. R., & Dimri, V. P. (2005). Depth determination from a non-stationary magnetic profile for scaling geology. *Geophysical Prospecting*, 53(3), 399–410. <https://doi.org/10.1111/j.1365-2478.2005.00480.x>
- Bansal, A. R., Gabriel, G., Dimri, V. P., & Krawczyk, C. M. (2011). Estimation of depth to the bottom of magnetic sources by a modified centroid method for fractal distribution of sources: An application to aeromagnetic data in Germany. *Geophysics*, 76(3), L11–L22. <https://doi.org/10.1190/1.3560017>
- Bhattacharyya, B. K., & Leu, L.-K. (1975a). Analysis of magnetic anomalies over Yellowstone National Park: Mapping of Curie point isothermal surface for geothermal reconnaissance. *Journal of Geophysical Research*, 80(32), 4461–4465. <https://doi.org/10.1029/JB080i032p04461>
- Bhattacharyya, B. K., & Leu, L.-K. (1975b). Spectral analysis of gravity and magnetic anomalies due to two-dimensional structures. *Geophysics*, 40(6), 993–1013. <https://doi.org/10.1190/1.1440593>
- Bialas, R. W., Buck, W. R., Studinger, M., & Fitzgerald, P. G. (2007). Plateau collapse model for the Transantarctic Mountains–West Antarctic Rift System: Insights from numerical experiments. *Geology*, 35(8), 687–690. <https://doi.org/10.1130/g23825a.1>
- Blakely, R. J. (1988). Curie temperature isotherm analysis and tectonic implications of aeromagnetic data from Nevada. *Journal of Geophysical Research*, 93(B10), 11817–11832. <https://doi.org/10.1029/JB093iB10p11817>
- Blakely, R. J. (1996). *Potential theory in gravity and magnetic applications*. Cambridge university press.
- Bouligand, C., Glen, J. M. G., & Blakely, R. J. (2009). Mapping Curie temperature depth in the Western United States with a fractal model for crustal magnetization. *Journal of Geophysical Research*, 114(B11), B11104. <https://doi.org/10.1029/2009JB006494>
- Brenn, G. R., Hansen, S. E., & Park, Y. (2017). Variable thermal loading and flexural uplift along the Transantarctic Mountains, Antarctica. *Geology*, 45(5), 463–466. <https://doi.org/10.1130/g38784.1>
- Burton-Johnson, A., Dziadek, R., & Martin, C. (2020). Review article: Geothermal heat flow in Antarctica: Current and future directions. *The Cryosphere*, 14(11), 3843–3873. <https://doi.org/10.5194/tc-14-3843-2020>
- Clauser, C., & Huenges, E. (1995). Thermal conductivity of rocks and minerals. In *Rock Physics & Phase Relations* (Vol. 3, pp. 105–126). <https://doi.org/10.1029/RF003p0105>
- Connard, G., Couch, R., & Gemperle, M. (1983). Analysis of aeromagnetic measurements from the Cascade Range in central Oregon. *Geophysics*, 48(3), 376–390. <https://doi.org/10.1190/1.1441476>
- Cook, C. P., Hemming, S. R., van de Fliert, T., Pierce Davis, E. L., Williams, T., Galindo, A. L., et al. (2017). Glacial erosion of East Antarctica in the Pliocene: A comparative study of multiple marine sediment provenance tracers. *Chemical Geology*, 466, 199–218. <https://doi.org/10.1016/j.chemgeo.2017.06.011>
- Davies, J. H. (2013). Global map of solid Earth surface heat flow. *Geochemistry, Geophysics, Geosystems*, 14(10), 4608–4622. <https://doi.org/10.1002/ggge.20271>
- DeConto, R. M., & Pollard, D. (2016). Contribution of Antarctica to past and future sea-level rise. *Nature*, 531(7596), 591–597. <https://doi.org/10.1038/nature17145>
- Drewry, D. J. (1976). Sedimentary basins of the East Antarctic craton from geophysical evidence. *Tectonophysics*, 36(1), 301–314. [https://doi.org/10.1016/0040-1951\(76\)90023-8](https://doi.org/10.1016/0040-1951(76)90023-8)
- Dziadek, R., Ferraccioli, F., & Gohl, K. (2021). High geothermal heat flow beneath Thwaites Glacier in West Antarctica inferred from aeromagnetic data. *Communications Earth & Environment*, 2(1), 162. <https://doi.org/10.1038/s43247-021-00242-3>
- Ebbing, J., Gernigon, L., Pascal, C., Olesen, O., & Osmundsen, P. T. (2009). A discussion of structural and thermal control of magnetic anomalies on the mid-Norwegian margin. *Geophysical Prospecting*, 57(4), 665–681. <https://doi.org/10.1111/j.1365-2478.2009.00800.x>
- Fahnestock, M., Abdalati, W., Joughin, I., Brozena, J., & Gogineni, P. (2001). High geothermal heat flow, basal melt, and the origin of rapid ice flow in Central Greenland. *Science*, 294(5550), 2338–2342. <https://doi.org/10.1126/science.1065370>
- Ferraccioli, F., Armadillo, E., Jordan, T. A., Bozzo, E., & Corr, H. (2009). Aeromagnetic exploration over the East Antarctic ice sheet: A new view of the Wilkes Subglacial Basin. *Tectonophysics*, 478(1), 62–77. <https://doi.org/10.1016/j.tecto.2009.03.013>
- Ferraccioli, F., Armadillo, E., Zunino, A., Bozzo, E., Rocchi, S., & Armiienti, P. (2009). Magmatic and tectonic patterns over the Northern Victoria Land sector of the Transantarctic Mountains from new aeromagnetic imaging. *Tectonophysics*, 478(1), 43–61. <https://doi.org/10.1016/j.tecto.2008.11.028>
- Ferraccioli, F., Coren, F., Bozzo, E., Zanolla, C., Gandolfi, S., Tabacco, I., & Frezzotti, M. (2001). Rifted(?) crust at the East Antarctic craton margin: Gravity and magnetic interpretation along a traverse across the Wilkes Subglacial Basin region. *Earth and Planetary Science Letters*, 192(3), 407–421. [https://doi.org/10.1016/S0012-821X\(01\)00459-9](https://doi.org/10.1016/S0012-821X(01)00459-9)
- Ferré, E. C., Friedman, S. A., Martín-Hernández, F., Feinberg, J. M., Till, J. L., Ionov, D. A., & Conder, J. A. (2014). Eight good reasons why the uppermost mantle could be magnetic. *Tectonophysics*, 624–625, 3–14. <https://doi.org/10.1016/j.tecto.2014.01.004>
- Finn, C. A., Goodge, J. W., Damaske, D., & Fanning, C. M. (2006). Scouting craton’s edge in paleo-pacific gondwana. In D. K. Fütterer, D. Damaske, G. Kleinschmidt, H. Miller, & F. Tessensohn (Eds.), *Antarctica: Contributions to global Earth sciences* (pp. 165–173). Springer Berlin Heidelberg. https://doi.org/10.1007/3-540-32934-X_20
- Fleming, T. H., Elliot, D. H., Foland, K. A., Jones, L. M., & Bowman, J. R. (1993). Disturbance of Rb-Sr and K-Ar isotopic systems in the Kirkpatrick basalt, north Victoria Land, Antarctica: Implications for middle cretaceous tectonism. In R. H. Findlay, R. Unrug, H. R. Banks, & J. J. Veever (Eds.), *Gondwana eight: Assembly, evolution and dispersal*. Balkema.
- Fox Maule, C., Purucker, M. E., Olsen, N., & Mosegaard, K. (2005). Heat flux anomalies in Antarctica revealed by satellite magnetic data. *Science*, 309(5733), 464–467. <https://doi.org/10.1126/science.1106888>
- Gambino, S., Armiienti, P., Cannata, A., Del Carlo, P., Giudice, G., Guiffrida, G., et al. (2021). Chapter 7.3 Mount Melbourne and Mount rittmann. *Geological Society*, 55, 741–758. <https://doi.org/10.1144/m55-2018-43>

- Goes, S., Hasterok, D., Schutt, D. L., & Klöcking, M. (2020). Continental lithospheric temperatures: A review. *Physics of the Earth and Planetary Interiors*, 306, 106509. <https://doi.org/10.1016/j.pepi.2020.106509>
- Golynsky, A. V., Ferraccioli, F., Hong, J. K., Golynsky, D. A., von Frese, R. R. B., Young, D. A., et al. (2018). New magnetic anomaly map of the Antarctic. *Geophysical Research Letters*, 45(13), 6437–6449. <https://doi.org/10.1029/2018GL078153>
- Goode, J. W. (2020). Geological and tectonic evolution of the Transantarctic Mountains, from ancient craton to recent enigma. *Gondwana Research*, 80, 50–122. <https://doi.org/10.1016/j.gr.2019.11.001>
- Goode, J. W., & Fanning, C. M. (2010). Composition and age of the East Antarctic shield in eastern Wilkes Land determined by proxy from oligocene-pleistocene glaciomarine sediment and Beacon Supergroup sandstones, Antarctica. *GSA Bulletin*, 122(7–8), 1135–1159. <https://doi.org/10.1130/b30079.1>
- Graw, J. H., Adams, A. N., Hansen, S. E., Wiens, D. A., Hackworth, L., & Park, Y. (2016). Upper mantle shear wave velocity structure beneath northern Victoria Land, Antarctica: Volcanism and uplift in the northern Transantarctic Mountains. *Earth and Planetary Science Letters*, 449, 48–60. <https://doi.org/10.1016/j.epsl.2016.05.026>
- Haggerty, S. E. (1978). Mineralogical constraints on Curie isotherms in deep crustal magnetic anomalies. *Geophysical Research Letters*, 5(2), 105–108. <https://doi.org/10.1029/GL005i002p00105>
- Hansen, S. E., Kenyon, L. M., Graw, J. H., Park, Y., & Nyblade, A. A. (2016). Crustal structure beneath the northern transantarctic mountains and Wilkes Subglacial Basin: Implications for tectonic origins. *Journal of Geophysical Research: Solid Earth*, 121(2), 812–825. <https://doi.org/10.1002/2015JB012325>
- Harris, C. R., Millman, K. J., van der Walt, S. J., Gommers, R., Virtanen, P., Cournapeau, D., et al. (2020). Array programming with NumPy. *Nature*, 585(7825), 357–362. <https://doi.org/10.1038/s41586-020-2649-2>
- Hasterok, D., Gard, M., & Webb, J. (2018). On the radiogenic heat production of metamorphic, igneous, and sedimentary rocks. *Geoscience Frontiers*, 9(6), 1777–1794. <https://doi.org/10.1016/j.gsf.2017.10.012>
- Huerta, A. D. (2007). Lithospheric structure across the transantarctic mountains constrained by an analysis of gravity and thermal structure (Vol. 1047. srp022). <https://doi.org/10.3133/of2007-1047.srp022>
- Hunter, J. (2007). Matplotlib: A 2D graphics environment. *Computing in Science & Engineering*, 9(3), 90–95. <https://doi.org/10.1109/MCSE.2007.55>
- Hussein, M., Mickus, K., & Serpa, L. F. (2013). Curie point depth estimates from aeromagnetic data from death valley and surrounding regions, California. *Pure and Applied Geophysics*, 170(4), 617–632. <https://doi.org/10.1007/s00024-012-0557-6>
- Idárraga-García, J., & Vargas, C. A. (2018). Depth to the bottom of magnetic layer in South America and its relationship to Curie isotherm, Moho depth and seismicity behavior. *Geodesy and Geodynamics*, 9(1), 93–107. <https://doi.org/10.1016/j.geog.2017.09.006>
- Jennings, S., Hasterok, D., & Payne, J. (2019). A new compositionally based thermal conductivity model for plutonic rocks. *Geophysical Journal International*, 219(2), 1377–1394. <https://doi.org/10.1093/gji/ggz376>
- Jordan, T. A., Ferraccioli, F., Armadillo, E., & Bozzo, E. (2013). Crustal architecture of the Wilkes Subglacial Basin in East Antarctica, as revealed from airborne gravity data. *Tectonophysics*, 585, 196–206. <https://doi.org/10.1016/j.tecto.2012.06.041>
- Kluyver, T., Ragan-Kelley, B., Pérez, F., Granger, B., Bussonnier, M., Frederi, J., et al. (2016). *Jupyter notebooks—A publishing format for reproducible computational workflows, positioning and power in academic publishing: Players, agents and agendas* (pp. 87–90). IOS Press.
- Kumar, R., Bansal, A. R., Betts, P. G., & Ravat, D. (2021). Re-assessment of the depth to the base of magnetic sources (DBMS) in Australia from aeromagnetic data using the defractal method. *Geophysical Journal International*, 225(1), 530–547. <https://doi.org/10.1093/gji/ggaa601>
- Lamarque, G., Bascou, J., Ménot, R.-P., Paquette, J.-L., Couzinié, S., Rolland, Y., & Cottin, J.-Y. (2018). Ediacaran to lower Cambrian basement in eastern George V Land (Antarctica): Evidence from UPb dating of gneiss xenoliths and implications for the South Australia–East Antarctica connection. *Lithos*, 318–319, 219–229. <https://doi.org/10.1016/j.lithos.2018.08.021>
- Langel, R. A., & Hinze, W. J. (1998). *The magnetic field of the Earth's lithosphere: The satellite perspective*. Cambridge University Press.
- Larour, E., Morlighem, M., Seroussi, H., Schiermeier, J., & Rignot, E. (2012). Ice flow sensitivity to geothermal heat flux of Pine Island Glacier, Antarctica. *Journal of Geophysical Research*, 117(F4), F04023. <https://doi.org/10.1029/2012JF002371>
- Lawrence, J. F., Wiens, D. A., Nyblade, A. A., Anandkrishnan, S., Shore, P. J., & Voigt, D. (2006). Crust and upper mantle structure of the Transantarctic Mountains and surrounding regions from receiver functions, surface waves, and gravity: Implications for uplift models. *Geochemistry, Geophysics, Geosystems*, 7(10). <https://doi.org/10.1029/2006GC001282>
- Leseane, K., Atekwana, E. A., Mickus, K. L., Abdelsalam, M. G., Shemang, E. M., & Atekwana, E. A. (2015). Thermal perturbations beneath the incipient Okavango Rift zone, northwest Botswana. *Journal of Geophysical Research: Solid Earth*, 120(2), 1210–1228. <https://doi.org/10.1002/2014JB011029>
- Li, C.-F., Lu, Y., & Wang, J. (2017). A global reference model of Curie-point depths based on EMAG2. *Scientific Reports*, 7(1), 45129. <https://doi.org/10.1038/srep45129>
- Li, C.-F., Zhou, D., & Wang, J. (2019). On application of fractal magnetization in Curie depth estimation from magnetic anomalies. *Acta Geophysica*, 67(5), 1319–1327. <https://doi.org/10.1007/s11600-019-00339-6>
- Lloyd, A. J., Wiens, D. A., Zhu, H., Tromp, J., Nyblade, A. A., Aster, R. C., et al. (2020). Seismic structure of the Antarctic upper mantle imaged with adjoint tomography. *Journal of Geophysical Research: Solid Earth*, 125(3). <https://doi.org/10.1029/2019JB017823>
- Llubes, M., Lanseau, C., & Rémy, F. (2006). Relations between basal condition, subglacial hydrological networks and geothermal flux in Antarctica. *Earth and Planetary Science Letters*, 241(3), 655–662. <https://doi.org/10.1016/j.epsl.2005.10.040>
- Lösing, M., & Ebbing, J. (2021). Predicting geothermal heat flow in Antarctica with a machine learning approach. *Journal of Geophysical Research: Solid Earth*, 126(6), e2020JB021499. <https://doi.org/10.1029/2020JB021499>
- Lösing, M., Ebbing, J., & Szwillus, W. (2020). Geothermal heat flux in Antarctica: Assessing models and observations by bayesian inversion. *Frontiers of Earth Science*, 8. <https://doi.org/10.3389/feart.2020.00105>
- Lösing, M., Moorkamp, M., & Ebbing, J. (2022). Joint inversion based on variation of information - a crustal model of Wilkes Land, east Antarctica. *Geophysical Journal International*, 232(1), 162–175. <https://doi.org/10.1093/gji/ggac334>
- Lucazeau, F. (2019). Analysis and mapping of an updated terrestrial heat flow data set. *Geochemistry, Geophysics, Geosystems*, 20(8), 4001–4024. <https://doi.org/10.1029/2019GC008389>
- Martos, Y. M., Catalán, M., Jordan, T. A., Golynsky, A., Golynsky, D., Eagles, G., & Vaughan, D. G. (2017). Heat flux distribution of Antarctica unveiled. *Geophysical Research Letters*, 44(22), 11–417. <https://doi.org/10.1002/2017GL075609>
- Martos, Y. M., Jordan, T. A., Catalán, M., Jordan, T. M., Bamber, J. L., & Vaughan, D. G. (2018). Geothermal heat flux reveals the Iceland hotspot track underneath Greenland. *Geophysical Research Letters*, 45(16), 8214–8222. <https://doi.org/10.1029/2018GL078289>
- Mather, B., & Delhay, R. (2019). PyCurious: A Python module for computing the Curie depth from the magnetic anomaly. *Journal of Open Source Software*, 4(39), 1544. <https://doi.org/10.21105/joss.01544>

- Mather, B., & Fulla, J. (2019). Constraining the geotherm beneath the British Isles from bayesian inversion of Curie depth: Integrated modelling of magnetic, geothermal, and seismic data. *Solid Earth*, 10(3), 839–850. <https://doi.org/10.5194/se-10-839-2019>
- Matsuoka, K., MacGregor, J. A., & Pattyn, F. (2012). Predicting radar attenuation within the Antarctic ice sheet. *Earth and Planetary Science Letters*, 359–360, 173–183. <https://doi.org/10.1016/j.epsl.2012.10.018>
- Maus, S., & Dimri, V. (1995). Potential field power spectrum inversion for scaling geology. *Journal of Geophysical Research*, 100(B7), 12605–12616. <https://doi.org/10.1029/95JB00758>
- Maus, S., Gordon, D., & Fairhead, D. (1997). Curie-temperature depth estimation using a self-similar magnetization model. *Geophysical Journal International*, 129(1), 163–168. <https://doi.org/10.1111/j.1365-246X.1997.tb00945.x>
- Maus, S., Lühr, H., Rother, M., Hemant, K., Balasis, G., Ritter, P., & Stolle, C. (2007). Fifth-generation lithospheric magnetic field model from CHAMP satellite measurements. *Geochemistry, Geophysics, Geosystems*, 8(5), Q05013. <https://doi.org/10.1029/2006GC001521>
- McKinney, W. (2010). Data structures for statistical computing in python. In *Proceedings of the 9th Python in Science Conference* (Vol. 445(1), pp. 51–56).
- Morelli, A., & Danesi, S. (2004). Seismological imaging of the Antarctic continental lithosphere: A review. *Global and Planetary Change*, 42(1), 155–165. <https://doi.org/10.1016/j.gloplacha.2003.12.005>
- Morlighem, M., Rignot, E., Binder, T., Blankenship, D., Drews, R., Eagles, G., et al. (2020). Deep glacial troughs and stabilizing ridges unveiled beneath the margins of the Antarctic ice sheet. *Nature Geoscience*, 13(2), 132–137. <https://doi.org/10.1038/s41561-019-0510-8>
- Núñez Demarco, P., Prezzi, C., & Sánchez Bettucci, L. (2020). Review of Curie point depth determination through different spectral methods applied to magnetic data. *Geophysical Journal International*, 224(1), 17–39. <https://doi.org/10.1093/gji/ggaa361>
- Okubo, Y., Graf, R. J., Hansen, R. O., Ogawa, K., & Tsu, H. (1985). Curie point depths of the Island of Kyushu and surrounding areas, Japan. *Geophysics*, 50(3), 481–494. <https://doi.org/10.1190/1.1441926>
- Olsen, N., Ravat, D., Finlay, C. C., & Kother, L. K. (2017). LCS-1: A high-resolution global model of the lithospheric magnetic field derived from CHAMP and swarm satellite observations. *Geophysical Journal International*, 211(3), 1461–1477. <https://doi.org/10.1093/gji/ggx381>
- Pappa, F., & Ebbing, J. (2021). *Gravity, magnetics and geothermal heat flow of the Antarctic lithospheric crust and mantle* (Vol. 56. M56-2020). Geological Society. <https://doi.org/10.1144/m56-2020-5>
- Pappa, F., Ebbing, J., & Ferraccioli, F. (2019). Moho depths of Antarctica: Comparison of seismic, gravity, and isostatic results. *Geochemistry, Geophysics, Geosystems*, 20(3), 1629–1645. <https://doi.org/10.1029/2018GC008111>
- Pattyn, F. (2010). Antarctic subglacial conditions inferred from a hybrid ice sheet/ice stream model. *Earth and Planetary Science Letters*, 295(3), 451–461. <https://doi.org/10.1016/j.epsl.2010.04.025>
- Pattyn, F., Carter, S. P., & Thoma, M. (2016). Advances in modelling subglacial lakes and their interaction with the Antarctic ice sheet. *Philosophical Transactions of the Royal Society A: Mathematical, Physical & Engineering Sciences*, 374(2059), 20140296. <https://doi.org/10.1098/rsta.2014.0296>
- Paxman, G. J. G., Jamieson, S. S. R., Ferraccioli, F., Bentley, M. J., Ross, N., Armadillo, E., et al. (2018). Bedrock erosion surfaces record former East Antarctic ice sheet extent. *Geophysical Research Letters*, 45(9), 4114–4123. <https://doi.org/10.1029/2018GL077268>
- Paxman, G. J. G., Jamieson, S. S. R., Ferraccioli, F., Bentley, M. J., Ross, N., Watts, A. B., et al. (2019). The role of lithospheric flexure in the landscape evolution of the Wilkes Subglacial Basin and transantarctic mountains, east Antarctica. *Journal of Geophysical Research: Earth Surface*, 124(3), 812–829. <https://doi.org/10.1029/2018JF004705>
- Perinelli, C., Gaeta, M., & Armentieri, P. (2017). Cumulate xenoliths from Mt. Overlord, northern Victoria Land, Antarctica: A window into high pressure storage and differentiation of mantle-derived basalts. *Lithos*, 268–271, 225–239. <https://doi.org/10.1016/j.lithos.2016.10.027>
- Pittard, M. L., Galton-Fenzi, B. K., Roberts, J. L., & Watson, C. S. (2016). Organization of ice flow by localized regions of elevated geothermal heat flux. *Geophysical Research Letters*, 43(7), 3342–3350. <https://doi.org/10.1002/2016GL068436>
- Pollard, D., DeConto, R. M., & Alley, R. B. (2015). Potential Antarctic Ice Sheet retreat driven by hydrofracturing and ice cliff failure. *Earth and Planetary Science Letters*, 412, 112–121. <https://doi.org/10.1016/j.epsl.2014.12.035>
- Purucker, M. (2013). Geothermal heat flux data set based on low resolution observations collected by the CHAMP satellite between 2000 and 2010, and produced from the MF-6 model following the technique described in Fox Maule et al. (2005). last access: 11 August 2022. Retrieved from <http://webserv.cs.umd.edu/isis/index.php>
- Ravat, D., Pignatelli, A., Nicolosi, I., & Chiappini, M. (2007). A study of spectral methods of estimating the depth to the bottom of magnetic sources from near-surface magnetic anomaly data. *Geophysical Journal International*, 169(2), 421–434. <https://doi.org/10.1111/j.1365-246X.2007.03305.x>
- Robinson, E. S., & Spletstoesser, J. F. (1986). Structure of the transantarctic mountains determined from geophysical surveys. In *Geology of the central transantarctic mountains* (pp. 119–162). <https://doi.org/10.1029/AR036p0119>
- Rossetti, F., Lisker, F., Storti, F., & Läufer, A. L. (2003). Tectonic and denudational history of the Rennick graben (north Victoria Land): Implications for the evolution of rifting between East and west Antarctica. *Tectonics*, 22(2). <https://doi.org/10.1029/2002TC001416>
- Salem, A., Green, C., Ravat, D., Singh, K. H., East, P., Fairhead, J. D., et al. (2014). Depth to Curie temperature across the central Red Sea from magnetic data using the de-fractal method. *Tectonophysics*, 624–625, 75–86. <https://doi.org/10.1016/j.tecto.2014.04.027>
- Schoof, C. (2007). Ice sheet grounding line dynamics: Steady states, stability, and hysteresis. *Journal of Geophysical Research*, 112(F3), F03S28. <https://doi.org/10.1029/2006JF000664>
- Shen, W., Wiens, D. A., Anandakrishnan, S., Aster, R. C., Gerstoft, P., Bromirski, P. D., et al. (2018). The crust and upper mantle structure of central and West Antarctica from bayesian inversion of Rayleigh wave and receiver functions. *Journal of Geophysical Research: Solid Earth*, 123(9), 7824–7849. <https://doi.org/10.1029/2017JB015346>
- Shen, W., Wiens, D. A., Lloyd, A. J., & Nyblade, A. A. (2020). A geothermal heat flux map of Antarctica empirically constrained by seismic structure. *Geophysical Research Letters*, 47(14), e2020GL086955. <https://doi.org/10.1029/2020GL086955>
- Sims, K. W. W., Aster, R. C., Gaetani, G., Blichert-Toft, J., Phillips, E. H., Wallace, P. J., et al. (2021). Chapter 7.2 Mount Erebus. *Geological Society, London, Memoirs*, 55(1), 695–739. <https://doi.org/10.1144/m55-2019-8>
- Smith, A. G., & Drewry, D. J. (1984). Delayed phase change due to hot asthenosphere causes Transantarctic uplift? *Nature*, 309(5968), 536–538. <https://doi.org/10.1038/309536a0>
- Sobh, M., Gerhards, C., Fadel, I., & Götze, H.-J. (2021). Mapping the thermal structure of southern Africa from Curie depth estimates based on wavelet analysis of magnetic data with uncertainties. *Geochemistry, Geophysics, Geosystems*, 22(11), e2021GC010041. <https://doi.org/10.1029/2021GC010041>
- Spector, A., & Grant, F. S. (1970). Statistical models for interpreting aeromagnetic data. *Geophysics*, 35(2), 293–302. <https://doi.org/10.1190/1.1440092>
- Stål, T., Reading, A. M., Halpin, J. A., & Whittaker, J. M. (2021). Antarctic Geothermal heat flow model: Aq1. *Geochemistry, Geophysics, Geosystems*, 22(2), e2020GC009428. <https://doi.org/10.1029/2020GC009428>

- Steed, R. N. (1983). Structural interpretations of Wilkes Land, Antarctica. *Antarctic earth science. International symposium*, 4.
- Stern, T. A., & ten Brink, U. S. (1989). Flexural uplift of the transantarctic mountains. *Journal of Geophysical Research*, 94(B8), 10315–10330. <https://doi.org/10.1029/JB094iB08p10315>
- Stokes, C. R., Abram, N. J., Bentley, M. J., Edwards, T. L., England, M. H., Foppert, A., et al. (2022). Response of the East Antarctic Ice Sheet to past and future climate change. *Nature*, 608(7922), 275–286. <https://doi.org/10.1038/s41586-022-04946-0>
- Studinger, M., Bell, R. E., Buck, W. R., Karner, G. D., & Blankenship, D. D. (2004). Sub-ice geology inland of the Transantarctic Mountains in light of new aerogeophysical data. *Earth and Planetary Science Letters*, 220(3), 391–408. [https://doi.org/10.1016/S0012-821X\(04\)00066-4](https://doi.org/10.1016/S0012-821X(04)00066-4)
- Szwillus, W., Baykiew, E., Dilixiati, Y., & Ebbing, J. (2022). Linearized Bayesian estimation of magnetization and depth to magnetic bottom from satellite data. *Geophysical Journal International*, 230(3), 1508–1533. <https://doi.org/10.1093/gji/ggac133>
- Tanaka, A., Okubo, Y., & Matsubayashi, O. (1999). Curie point depth based on spectrum analysis of the magnetic anomaly data in East and Southeast Asia. *Tectonophysics*, 306(3), 461–470. [https://doi.org/10.1016/S0040-1951\(99\)00072-4](https://doi.org/10.1016/S0040-1951(99)00072-4)
- Telford, W. M., Geldart, L. P., & Sheriff, R. E. (1990). *Applied geophysics*. Cambridge University Press.
- ten Brink, U. S., Hackney, R. I., Bannister, S., Stern, T. A., & Makovsky, Y. (1997). Uplift of the transantarctic mountains and the bedrock beneath the East Antarctic ice sheet. *Journal of Geophysical Research*, 102(B12), 27603–27621. <https://doi.org/10.1029/97JB02483>
- ten Brink, U. S., & Stern, T. (1992). Rift flank uplifts and hinterland basins: Comparison of the transantarctic mountains with the great escarpment of southern Africa. *Journal of Geophysical Research*, 97(B1), 569–585. <https://doi.org/10.1029/91JB02231>
- Todoschuck, J. P., Pilkington, M., & Gregotski, M. E. (1992). If geology is fractal, what do we do next? *The Leading Edge*, 11(10), 29–35. <https://doi.org/10.1190/1.1436848>
- Treitel, S., Clement, W. G., & Kaul, R. K. (1971). The spectral determination of depths to buried magnetic basement rocks. *Geophysical Journal International*, 24(4), 415–428. <https://doi.org/10.1111/j.1365-246X.1971.tb02187.x>
- Turcotte, D. L., & Schubert, G. (2002). *Geodynamics*. Cambridge university press.
- Van Liefferinge, B., Pattyn, F., Cavitte, M. G. P., Karlsson, N. B., Young, D. A., Sutter, J., & Eisen, O. (2018). Promising Oldest Ice sites in East Antarctica based on thermodynamical modelling. *The Cryosphere*, 12(8), 2773–2787. <https://doi.org/10.5194/tc-12-2773-2018>
- Virtanen, P., Gommers, R., Oliphant, T. E., Haberland, M., Reddy, T., Cournapeau, D., et al. (2020). SciPy 1.0: Fundamental algorithms for scientific computing in Python. *Nature Methods*, 17(3), 261–272. <https://doi.org/10.1038/s41592-019-0686-2>
- Wang, Y., & Hou, S. (2009). A new interpolation method for Antarctic surface temperature. *Progress in Natural Science*, 19(12), 1843–1849. <https://doi.org/10.1016/j.pnsc.2009.07.012>
- Wannamaker, P., Hill, G., Stodt, J., Maris, V., Ogawa, Y., Selway, K., et al. (2017). Uplift of the central transantarctic mountains. *Nature Communications*, 8(1), 1588. <https://doi.org/10.1038/s41467-017-01577-2>
- Wasilewski, P. J., Thomas, H. H., & Mayhew, M. A. (1979). The Moho as a magnetic boundary. *Geophysical Research Letters*, 6(7), 541–544. <https://doi.org/10.1029/GL006i007p00541>
- Whitehouse, P. L., Gomez, N., King, M. A., & Wiens, D. A. (2019). Solid Earth change and the evolution of the Antarctic ice sheet. *Nature Communications*, 10(1), 503. <https://doi.org/10.1038/s41467-018-08068-y>
- Wiens, D. A., Shen, W., & Lloyd, A. J. (2021). *The seismic structure of the Antarctic upper mantle* (Vol. 56. M56-2020). Geological Society. <https://doi.org/10.1144/m56-2020-18>
- Winkelmann, R., Martin, M. A., Haseloff, M., Albrecht, T., Bueler, E., Khroulev, C., & Levermann, A. (2011). The potsdam parallel ice sheet model (PISM-PIK) – Part 1: Model description. *The Cryosphere*, 5(3), 715–726. <https://doi.org/10.5194/tc-5-715-2011>
- Winsborrow, M. C. M., Clark, C. D., & Stokes, C. R. (2010). What controls the location of ice streams? *Earth-Science Reviews*, 103(1), 45–59. <https://doi.org/10.1016/j.earscirev.2010.07.003>
- Yamasaki, T., Miura, H., & Nogi, Y. (2008). Numerical modelling study on the flexural uplift of the Transantarctic Mountains. *Geophysical Journal International*, 174(1), 377–390. <https://doi.org/10.1111/j.1365-246X.2008.03815.x>